

1 Radiative convective equilibrium over a land  
2 surface

3  
4 Nicolas Rochetin  
5 Columbia University  
6 New York, NY 10027  
7

8 Benjamin R. Lintner  
9 Rutgers, the State University of New Jersey  
10 New Brunswick, NJ 08901  
11

12 Kirsten L. Findell  
13 Geophysical Fluid Dynamics Laboratory  
14 Princeton, NJ 08542  
15

16 Adam H. Sobel  
17 Columbia University  
18 New York, NY 10027  
19

20 Pierre Gentine<sup>1</sup>  
21 Columbia University  
22 New York, NY 10027  
23

---

<sup>1</sup> Corresponding author: Pierre Gentine, Earth Institute / Department of Earth and Environmental Engineering, Columbia University, 500 W 120th St., New York, NY 10027, email: [pg2328@columbia.edu](mailto:pg2328@columbia.edu)

## 24 Abstract

25 Radiative-convective equilibrium (RCE) describes an idealized state of the atmosphere  
26 in which the vertical temperature profile is determined by a balance between radiative  
27 and convective fluxes. While RCE has been applied extensively over oceans, its  
28 application over the land surface has been limited. The present study explores the  
29 properties of RCE over land using an atmospheric single column model (SCM) from the  
30 Laboratoire de Meteorologie Dynamique (LMD) General Circulation Model (LMDZ5B)  
31 coupled in temperature and moisture to a land surface model comprising a simplified  
32 bucket model with finite moisture capacity. Given the presence of a large-amplitude  
33 diurnal heat flux cycle, the resultant RCE exhibits multiple equilibria when conditions are  
34 neither strictly water- nor energy-limited. By varying top-of-the-atmosphere insolation  
35 (through changes in latitude), total system water content, and initial temperature  
36 conditions, the sensitivity of the land RCE states is assessed, with particular emphasis  
37 on the role of clouds. Based on this analysis, it appears that a necessary condition for  
38 the model to exhibit multiple equilibria is the presence of low-level clouds coupled to the  
39 diurnal cycle of radiation. In addition the simulated surface precipitation rate varies non-  
40 monotonically with latitude as a result of a tradeoff between in-cloud rain rate and  
41 subcloud rain re-evaporation, thus underscoring the importance of subcloud layer  
42 processes and unsaturated downdrafts. It is shown that clouds, especially at low levels,  
43 are key elements of the internal variability of the coupled land-atmosphere system  
44 through their feedback on radiation.

45

## 46 1. Introduction

47 The concept of radiative-convective equilibrium (RCE) was introduced by  
48 Manabe and Wetherald (1967), following the earlier work of Gold (1909) and Goody  
49 (1949), to describe an idealized, statistical state of the atmosphere in which a balance  
50 between radiative cooling and convective heating determines the vertical temperature  
51 profile. RCE postulates that, on average, convective scale motions compensate for the  
52 destabilization of the atmosphere by radiation. RCE represents a powerful tool for  
53 estimating convective sensitivity to ocean surface temperature and for diagnosing the  
54 possible mechanisms through which deep convection is maintained and interacts with  
55 the surface fluxes in the absence of large-scale flow. RCE has been applied to a wide  
56 range of problems, including estimation and scaling of convective mass fluxes  
57 (Tompkins and Craig 1998a), the organization of tropical deep convection (Tompkins  
58 and Craig 1998b, Tompkins 2001a,b) and climate sensitivity to greenhouse gas forcing  
59 (Muller et al. 2011; Romps 2011).

60 In most of the applications of RCE in either single column models (SCMs) or  
61 cloud resolving models (CRMs), the surface boundary has been an ocean, often with  
62 prescribed surface temperature. Complications over land stem from the greater  
63 complexity associated with interacting components such as vegetation, soil moisture,  
64 and soil temperature. However, some studies have simplified the land system to  
65 address these complications. For instance, RCE has been considered for a swamp  
66 surface (Manabe and Wetherald 1967; Renno 1997) or with a constrained hydrologic  
67 cycle (i.e. with prescribed evapotranspiration) and nudging of 10 cm soil temperature  
68 toward a prescribed value (Prigent et al., 2011). Tompkins and Craig (1998a) and

69 Schlemmer et al. (2011) performed an experiment involving a CRM coupled to land  
70 surface in which the system achieves a "diurnal equilibrium" state, i.e. a quasi-stationary  
71 regime in which the surface and the boundary layer temperatures exhibit diurnal  
72 oscillations. In these studies, the soil and atmospheric temperature profiles were  
73 relaxed toward climatological values at points far from the surface.

74 In our study, we consider an extension of the concept of RCE applied to a land  
75 surface with a closed (water-conserving) hydrologic budget. As far as we are aware,  
76 ours is the first study to evaluate equilibrium land-atmosphere coupling in an SCM fully  
77 coupled to a land surface model. Of particular interest in our exploration of RCE over  
78 land is the potential existence of multiple equilibria. For prescribed-SST conditions, the  
79 RCE state is uniquely determined by the SST and radiative forcing, i.e., in the absence  
80 of energy exchange through the surface (and associated advective transport), the  
81 isolated, fixed SST RCE system possesses a unique equilibrium solution (Hilbert 1912;  
82 Tompkins and Craig 1998b; Renno 1997), with the ocean acting as both a thermostat  
83 and an infinite water source. On the other hand, Renno (1997) and Tompkins (2001a,b)  
84 showed that introduction of a surface hydrologic cycle through a swamp ocean, in which  
85 the surface temperature is interactively determined through the balance of surface  
86 fluxes assuming zero soil heat capacity, permits the existence of multiple equilibria.  
87 Even if multiple equilibria are not realized in the real climate system, e.g., because of  
88 the presence of internal variability or seasonal evolution, they may nonetheless provide  
89 insights regarding the evolution of the coupled land-atmosphere system.

90 Over land the existence of multiple equilibria has been explored in the context of  
91 land-atmosphere feedbacks. For instance, large-scale continental recycling forced by

92 stochastic advection exhibits two distinct equilibria comprising dry and moist surface  
93 states (Rodríguez-Iturbe et al. 1991a,b; Entekhabi et al. 1992). Land and boundary-  
94 layer interactions can also induce bimodality in the surface Bowen ratio (Entekhabi and  
95 Brubaker 1995; Brubaker and Entekhabi 1995). Similarly, Wang and Eltahir (2000)  
96 demonstrated the emergence of multiple equilibria in simulations of the West African  
97 climate including biosphere-atmosphere interactions. The Global Land Atmosphere  
98 Coupling Experiment (GLACE; Koster et al. 2004) suggests the existence of land-  
99 atmosphere coupling hotspots, which typically occur in the transition zones between  
100 arid and humid regions. The physical mechanisms that produce such hotspots are still  
101 not completely understood, although some progress has been made using some  
102 simplified analysis of the land surface coupled to the atmosphere (e.g. Guo et al. 2006;  
103 Koster et al. 2006; DelSole et al. 2009, Lintner et al. 2013). Recently, Aleina et al.  
104 (2013) demonstrated the emergence of multiple equilibria (desert or forest) for a toy  
105 model of a planet when interactive vegetation is included.

106         Apart from the GCM-based analyses of GLACE, most studies of the feedbacks of  
107 soil moisture and precipitation over land have been performed over relatively short time  
108 scales from one to several days (Hohenegger et al. 2009; Seneviratne et al. 2010;  
109 Gentine et al. 2013), or by aggregating diurnal-scale processes over the summer  
110 season (D’Odorico and Porporato 2004; Findell et al. 2011). A key challenge for the  
111 analysis of observations and complex GCMs is that weather and climate variability may  
112 overwhelm or otherwise mask signatures of land-atmosphere coupling (Phillips and  
113 Klein 2014). Thus, we believe that analyses performed using idealized frameworks such  
114 as the model considered here can stimulate improved understanding of long-term

115 (seasonal, annual) land-atmosphere interactions: what such analyses may lack in terms  
116 of realism is leveraged against the ease and transparency of diagnosis.

117         The paper is structured as follows. Section 2 provides an overview of the  
118 Laboratoire de Meteorologie Dynamique (LMD) General Circulation Model (LMDZ5B)  
119 SCM used in this study and the experimental setup employed to obtain RCE solutions  
120 over land. In section 3, we document the existence of multiple equilibria in a set of  
121 experiments in which we vary latitude, total (soil plus atmosphere) moisture content,  
122 and initial soil temperature, while Section 4 provides a more in-depth analysis of the  
123 RCE solutions and how these relate to land surface, cloud-radiative, and convective  
124 processes in the model. In section 5, we present the results of sensitivity experiments to  
125 assess how the diurnal cycle of radiation and cloud radiative feedbacks impact the  
126 existence of multiple equilibria. The final section summarizes the key findings of this  
127 study and discusses some implications of land region RCE for interpreting land region  
128 climate.

## 129 2. Model description and setup:

### 130         **2.1. Model description:**

#### 131                 2.1.1. Atmosphere

132         We use the SCM version of the LMDZ5B GCM developed by the Laboratoire de  
133 Meteorologie Dynamique (Hourdin et al. 2012). LMDZ5B has been used to perform  
134 climate simulations for the IPCC 5th assessment report. Here we give a brief description  
135 of the model; the reader is referred to Hourdin et al. (2012) for a more extensive  
136 discussion.

137           The model has 39 nonuniformly-spaced levels in the vertical. The first grid point  
138 is at 35 m, with 8 grid-points distributed in the first kilometer. Between 1 and 20 km, the  
139 mean vertical resolution is 800 m and the model top is located at 40 km. Separate  
140 parameterizations of shallow and deep convection are included. For shallow convection,  
141 the eddy diffusive scheme of Mellor and Yamada (1994) is combined with a mass-flux  
142 representation of boundary-layer thermals (Hourdin et al. 2002; Rio and Hourdin 2008;  
143 Rio et al. 2010) to account for, respectively, turbulence in the surface and inversion  
144 layers, and non-local convective transport induced by boundary layer coherent  
145 structures. Thermals are represented using a bulk entraining-detraining plume approach  
146 (Simpson and Wiggert 1969; Betts 1973) to compute the properties of a mean  
147 characteristic thermal representing the dry and cloudy (if saturation level is reached)  
148 boundary-layer thermals present in a model grid-cell. The plume model diagnoses the  
149 heights of cumulus base and top, as well as the vertical profiles of the plume vertical  
150 velocity, thermodynamic properties and fractional coverage, through the vertical  
151 evolution of mass flux.

152           Emanuel's deep convection scheme (Emanuel 1991) is added to this scheme for  
153 the treatment of precipitating-deep convection. The scheme has been modified by  
154 Grandpeix and Phillips (2004) to improve the sensitivity of the simulated deep  
155 convection to tropospheric relative humidity (Derbyshire et al. 2004). The triggering  
156 criterion of deep convection is based on the concept of available lifting energy (*ALE*)  
157 provided by boundary-layer thermals: deep convection is triggered whenever *ALE*  
158 overcomes the convective inhibition (*CIN*). A cold pool (or wake) parameterization has  
159 also been added to Emanuel's scheme with cold pools fed by the unsaturated

160 downdrafts resulting from rain re-evaporation (Betts 1976; Tompkins 2001b) outside the  
161 cloud. These cold pools also provide updraft lifting energy that may re-trigger deep  
162 convection by exceeding the  $C/N$  (Tompkins 2001b). The closure follows Grandpeix and  
163 Lafore (2010) and relates the cloud-base mass flux to the available lifting power ( $ALP$ )  
164 provided by subcloud processes,  $C/N$ , and the vertical velocity at the level of free  
165 convection (see details in Grandpeix et al. 2010; Grandpeix and Lafore 2010).

166 In the LMDZ GCM, precipitation is divided into (1) a convective part, generated  
167 by Emanuel's convection scheme (i.e. cumulonimbus clouds); and a (2) stratiform part,  
168 generated by (i) large-scale condensation related to a grid-scale ascent, (ii) boundary-  
169 layer thermal plumes related to cumulus clouds and (iii) turbulent diffusion related to  
170 fog. However since there is no large-scale ascent in the present RCE SCM framework,  
171 clouds and precipitation are completely determined by the parameterized subgrid-scale  
172 processes, i.e. turbulence, shallow convection and deep convection. The radiation  
173 scheme (Morcrette 1991) fully interacts with clouds and other components of the  
174 atmosphere. In LMDZ5B, maximum cloud overlapping is applied to compute radiative  
175 forcing when adjacent layers are cloudy, as for cumulus clouds, whereas the random  
176 overlapping is applied when two cloudy layers are separated by at least one clear layer,  
177 as for stratiform clouds.

178 For both stratiform and convective clouds, cloud cover is computed following a  
179 statistical cloud scheme with a log-normal probability density function, representing the  
180 subgrid-scale variability of total water content (Bony and Emanuel 2001). In this  
181 scheme, the in-cloud water content  $q_{inc}$ , condensed water  $q_c$  and cloud fraction are  
182 deduced from the distribution and average saturation of specific humidity. In the current

183 standard version of LMDZ5B, ice thermodynamics is not taken into account in the deep  
184 convection scheme. Inclusion of ice increases the cold pool intensity and thereby  
185 strengthens deep convection via the *ALP* closure, although this has been found to have  
186 little effect on upper level heating rates.

### 187 2.1.2. Soil Model

188 The soil model uses a diffusion scheme for heat propagation, assuming a  
189 diffusivity of  $1.06 \times 10^{-6} \text{ m}^2 \text{ s}^{-1}$ . A zero ground heat flux condition is imposed at infinite  
190 depth. The dynamics of soil water content  $Q_{soil}$  is represented with a simple bucket  
191 model (Manabe, 1969, Koster and Suarez 1994), and includes precipitation,  
192 evaporation and runoff generation. A soil saturation threshold is prescribed at  $Q_{max}$   
193 =1.5m, above which the excess of water is removed completely via runoff. Under these  
194 conditions, total water content of the land-atmosphere system,  $Q_{tot} = Q_{soil} + W$ , where  
195  $W$  is precipitable water, is no longer conserved. However, in our experiments,  $Q_{max}$  is set  
196 to a sufficiently large value (1.5m) to avoid runoff and therefore non-conservation.  
197 Physically  $Q_{max}$  corresponds to an effective rooting depth (Rodríguez-Iturbe et al. 1999;  
198 Laio et al. 2001) although the model contains no explicit representation of vegetation.  
199 The surface albedo is taken as  $\alpha=0.19$ . Although this highly reduced soil model may  
200 affect the coupling between the soil and the atmosphere, we show below that the  
201 simplified system still permits nonlinearities and multiple equilibria.

### 202 2.1.3. Surface Fluxes

203 Sensible heat flux and evaporation are computed via bulk formulations:

204  $\phi_{sens} = \rho V_0 C_{d,v} C_{d,h} (T_s - T_1)$  and  $Evap = \beta E_{pot}$  with  $E_{pot}$  the potential evaporation computed

205 as  $E_{\text{pot}} = \rho V_0 C_{d,v} C_{d,h} (q_{\text{sat},T_s} - q_1)$  and  $\beta$  the evapotranspiration coefficient reflecting linear  
206 soil moisture stress. Here,  $\rho=1.17 \text{ kg/m}^3$  is the surface air density,  $V_0$  is the first level  
207 wind speed,  $C_{d,v}$  the neutral drag coefficient for a land surface,  $C_{d,h}$  the stability  
208 correction based on the local Richardson number (see Hourdin et al. 2012),  $C_p=1004 \text{ J}$   
209  $\text{K}^{-1} \text{ kg}^{-1}$  is the dry air heat capacity,  $T_s$  the surface skin temperature,  $T_1$  the first  
210 atmospheric layer temperature,  $q_{\text{sat},T_s}$  the saturation specific humidity at the surface, and  
211  $q_1$  the first layer specific humidity.  $\beta$  varies linearly between 0 and 1 for soil moisture  
212 content between  $Q_{\text{soil}}$  and  $Q_{\text{max}}/2$  and saturates at  $\beta=1$  for  $Q_{\text{soil}} > Q_{\text{max}}/2$ . This  
213 relationship actually mimics idealized vegetation, for which stomatal opening depends  
214 quasi-linearly on soil moisture up to a maximum value (saturation) (Porporato et al.  
215 2001). If  $Q_{\text{soil}} > Q_{\text{max}}$ , runoff is generated to maintain  $Q_{\text{soil}} = Q_{\text{max}}$  (see previous  
216 subsection).

## 217 **2.2. Methodology:**

218 The LMDZ5B SCM is integrated for 10 years with a time step  $\Delta t = 450 \text{ s}$ , LMDZ  
219 standard time step used for CMIP5 simulations. An initial atmospheric profile (extracted  
220 from the First ISCCP Regional Experiment - FIRE - campaign, see Cox *et al.* 1987) is  
221 prescribed, as well as initial, vertically uniform, ground temperature  $T_0$  and soil moisture  
222  $Q_0$ . The RCE framework is applied without large-scale velocity or tendencies, as in most  
223 prior studies of oceanic RCE. A diurnal cycle of incoming solar radiation is imposed at  
224 TOA, corresponding to the annual mean value at the prescribed latitude. The model  
225 computes a residual surface wind, driven by convective-scale motions, that maintains  
226 consistent surface fluxes. Over oceanic surfaces, some surface wind must be included

227 to ensure heat and moisture transfer; indeed, surface wind provides the mechanical  
228 forcing (forced convection) that critically contributes to surface fluxes over oceans. Over  
229 land, however, daytime heating of the surface provides surface buoyancy instability  
230 (free convection) that thermally drives surface energy exchanges. Thus, surface wind is  
231 much less critical over lands than over the ocean. In section 5, we perform a sensitivity  
232 analysis on the impact of relaxing the atmosphere toward a nonzero geostrophic wind  
233 and found that it does not modify the conclusions reached here.

234 The sensitivity experiments discussed in the following sections consider changes  
235 in (i) latitude,  $\lambda$ ; (ii) total water content,  $Q_{tot}$ ; and (iii) initial ground temperature,  $T_0$ . Note  
236 that variation of total water content is performed by varying the initial soil water content  
237  $Q_0$  while maintaining the same initial precipitable water  $W_0 = 25 \text{ kg/m}^2$ .

### 238 **2.3. Characteristics of the baseline LMDZ5B RCE state:**

239 We run the model for the following baseline conditions:  $\lambda=35^\circ$ ,  $T_0=300\text{K}$ ,  $Q_{tot} = 40$   
240 mm (i.e.  $Q_0 = 15 \text{ mm}$ ). When the soil-atmosphere system reaches TOA radiative  
241 equilibrium, a diurnal-mean equilibrium surface temperature is reached. The system  
242 may require several years to achieve equilibrium because of the large soil depth and its  
243 corresponding thermal inertia. In this study, we assume that 10 years is a sufficiently  
244 long period for the soil to approximately equilibrate with the atmosphere, i.e. with an  
245 imbalance inferior to  $4 \text{ W/m}^2$ .

246 The atmosphere is in RCE when the net atmospheric radiative cooling balances  
247 the net convective heating. In fact, an atmospheric equilibrium is reached within a few  
248 weeks (see Fig 1a) and thereafter holds throughout most of the simulation. Indeed, the  
249 daily-averaged time series of the radiative cooling ( $Q_{rad}$ ) and convective heating ( $Q_{con}$ )

250 profile nearly balance each other. The time scale of convection (few hours) is much  
251 shorter than the radiative time scale (around 40 days), so any fluctuation in the surface  
252 energy or TOA radiation budgets is rapidly eliminated by convection (Cronin and  
253 Emanuel, 2013). Consequently, on daily timescales the integrated atmospheric energy  
254 budget is zero in all simulations at equilibrium, as depicted by the solid line in Fig 1b. In  
255 other words, RCE guarantees the same net energy flux at the surface and at TOA since  
256 there is no energy accumulation in the atmosphere. Consequently, the dashed line in  
257 Fig 1b not only represents the net energy flux but also the net energy flux at TOA.  
258 Periods where the two curves are superimposed in Fig 1b correspond to periods where  
259 the atmospheric energy loss (gain) corresponds to a similar energy gain (loss) for the  
260 soil. However, because of its large depth, the soil requires some time to balance  
261 atmospheric perturbations and the whole soil-atmosphere system may not be at  
262 equilibrium. For example, in simulation year 1984, the atmosphere experiences a strong  
263 perturbation that induces a departure from the preceding RCE state. This large  
264 atmospheric fluctuation drives a soil response at longer timescales through a surface  
265 temperature increase (see Fig 1c). Again before the final stable RCE is reached, the  
266 entire land-atmosphere system may be out of equilibrium as the soil column adjusts. In  
267 this unstable regime, the inherent system internal variability can generate jumps from  
268 one equilibrium state to another one. Hence, the system can pass through different  
269 equilibria states before reaching its final steady RCE solution. Hereafter, we only  
270 consider the RCE state reached after 10 years of simulation (assuming it is close  
271 enough to the final RCE).

272 Fig 2 depicts the diurnal course of energy fluxes for the control run (CTL). The  
273 bucket soil model (bucket) used in the LMDZ5B SCM may be compared with a slab  
274 ocean model with a small heat capacity, which allows diurnal variations in surface  
275 temperature, but with a larger Bowen ratio and limited water holding capacity. Because  
276 of the small thermal soil inertia the system oscillates around the equilibrium state on  
277 daily timescales (see Fig 2a).

278 As already seen in Fig 1, the surface and TOA energy budgets are close to zero  
279 in the baseline simulation. The RCE over a land surface reaches a steady periodic  
280 regime, in which the diurnal solar forcing drives a periodic response of the land-  
281 atmosphere system, both in terms of surface temperature and precipitation as seen in  
282 Fig 2a and Fig 2b. At equilibrium, surface temperature and precipitation exhibit very little  
283 day-to-day variability (not shown). The diurnal cycle of  $T_s$  exhibits a 1- to 2-hour lag  
284 with respect to solar forcing, which is characteristic of land surfaces for which the  
285 maximum is typically reached between 1300 LT and 1600 LT (Gentine et al. 2010).  
286 Regarding precipitation, prior studies have documented the presence of an afternoon  
287 peak in land region precipitation, especially in the tropics, in observations and CRMs  
288 (e.g. Bechtold et al. 2004; Guichard et al. 2004; Dai 2006; Rio et al. 2009, 2012). Thus,  
289 the land region RCE in the LMDZ5B SCM produces consistent diurnal cycle phasing  
290 relative to observations and high-resolution models.

291 After 10 years of simulation, RCE applies to daily averages. Fig 2c demonstrates  
292 that the subdaily (hourly) behavior deviates from RCE. The maximum soil heating  
293 occurs early in the morning, when turbulent fluxes are relatively weak and cannot  
294 dissipate much of the radiative input; rather, most of the heating at this time is

295 dissipated as ground heat flux (Gentine et al. 2011; 2012). In terms of hydrologic cycle,  
296 the daily-averaged precipitation and evaporation balance each other with surface  
297 precipitation rates across the suite of simulations ranging from one to three  
298 mm/day (discussed below).

299 Fig 2d depicts the diurnal evolution of radiative and convective heating integrated  
300 over the atmospheric column. Convective heating exhibits a strong diurnal cycle  
301 imposed by the large-amplitude diurnal variations in surface turbulent heat fluxes. The  
302 net radiative energy budget of the atmosphere is positive between 9 and 15 LT because  
303 of the large shortwave absorption. Diurnal variations in longwave tendencies are an  
304 order of magnitude smaller than the shortwave ones. Continental RCE is thus achieved  
305 for daily averages: the atmosphere experiences a net heating during daylight hours  
306 compensated by an equivalent net cooling at night. This is a key difference with a  
307 prescribed-SST framework over the ocean, in which the fixed SST ensures a permanent  
308 energy balance (i.e. verified at each instant), with continuous precipitation. The large  
309 diurnal cycle over land surfaces, induced by the low continental heat capacity compared  
310 to the ocean, provides increased surface variability compared to the oceanic case with  
311 prescribed SST. Even at equilibrium there can be substantial subdiurnal changes in  
312 surface temperature, boundary layer depth, cloud cover, and convection, which can  
313 respond nonlinearly to the diurnal course of radiation. This added variability appears to  
314 play a role in determining the equilibrium states (Rodriguez-Iturbe et al. 1991), as will be  
315 seen in section 5. The addition of the surface hydrological cycle, which limits the  
316 amount of available water at the surface, also increases the system's degrees of  
317 freedom compared to the prescribed-SST RCE. The energy in the system is thus

318 controlled by the latitude (and prescribed planetary albedo), and the hydrologic cycle is  
319 constrained by the initial total water content  $Q_0$ .

### 320 3. Existence of multiple equilibria

321 The sensitivity of RCE to changes in solar forcing, total moisture and initial  
322 surface temperature is investigated by modifying three parameters: the latitude  $\lambda$ , the  
323 total water content  $Q_{tot}$ , through specification of initial soil water content  $Q_0$ , and initial  
324 ground temperature  $T_0$ . Each pair of latitude and total water contents may be viewed as  
325 distinct climatological conditions.  $\lambda$  ranges from  $30^\circ$  to  $40^\circ$  in increments of  $2.5^\circ$ . As we  
326 will see in the following, this range is sufficient to cover the entire spectrum of possible  
327 RCE states. The initial  $Q_0$  ranges from 5 mm to 45 mm in increments of 10 mm, or  
328 equivalently,  $Q_{tot}$ , ranges from 30 mm to 70 mm. For each of the 25 climate states, the  
329 LMDZ5B SCM is initialized with one of 5 values of  $T_0$  ranging from 280 K to 320 K with  
330 an increment of 10 K, giving a total of 125, 10-year simulations. Note that all other  
331 model parameters are set to the baseline values. In what follows, we describe each  
332 simulation's final state by its mean equilibrium surface temperature (K) and soil water  
333 content (mm). For some latitude and total water content pairs, distinct final states are  
334 obtained with different initial ground temperatures. Thus, the coupled soil-atmosphere  
335 system exhibits multiple equilibria (see next section).

336 Fig. 3 provides an overview of the RCE combinations for the different  $\lambda$ ,  $T_0$ , and  
337  $Q_0$ . Before discussing the sensitivity analysis, we point out that a strong negative  
338 correlation exists between equilibrium soil surface temperature  $T_s$  and soil moisture  
339 content  $Q_{soil}$ . In the simplified bucket land surface hydrology the evapotranspiration

340 efficiency  $\beta$  increases linearly with soil moisture (see section 2.1.2.). Low  $Q_{soil}$  generates  
341 low evaporation, so most of the net radiative heating at the surface must be balanced by  
342 sensible heat flux (or ground heat flux). On the other hand, latent heat release is a more  
343 efficient heat transfer mechanism than other heat fluxes at medium to high temperature  
344 (Bateni and Entekhabi 2012). For low soil moisture, surface temperature quickly rises  
345 since the available cooling mechanisms are not efficient. Such behavior is well known  
346 for the daily variations of surface skin temperature and is used as an indicator of water  
347 stress (Bastiaanssen et al. 1998; Castelli et al. 1999; Boulet et al. 2007).

348 No multiple equilibria are seen at either high ( $\lambda = 40^\circ$ ) or low ( $\lambda = 30^\circ$ ) latitudes.  
349 For these latitudes, the RCE is either “warm and dry surface” (see Fig 3 red symbols) or  
350 “cool and wet surface” (Fig 3 blue symbols). The warm-dry RCE corresponds to a high  
351 surface temperature associated with a nearly dry soil ( $Q_{soil} < 5$  mm), while the cool-wet  
352 RCE corresponds to a low surface temperature associated with a high soil water  
353 content and low precipitable water ( $W \sim 5$  mm). The warm and cool RCE equilibria can  
354 be found at all latitudes and total water contents. In other words, for any latitude and  
355 total water content, there is at least one  $T_0$  that can lead to a warm-dry or a cool-wet  
356 solution. However, the warm-dry and cool-wet solutions can exhibit different surface  
357 temperatures depending on the solar forcing and water availability.

358 As seen in Figure 4 as an example, for  $Q_0 = 5$  mm (i.e.  $Q_{tot} = 30$ mm) increasing  
359 latitude (i) favors cool solutions and (ii) leads to a monotonic decrease of final soil  
360 temperature for both warm and cool solutions. Moreover, the sensitivity of the  
361 equilibrium solution to a change in latitude is more pronounced for warm solutions.  
362 Indeed, the final  $T_s$  ranges from 274 K to 278 K for the cool states, whereas it ranges

363 from 296 K to 306 K for the warm solutions. Sensitivity to  $Q_0$  is nontrivial: at the extreme  
364 latitudes, the warm RCE state ( $\lambda = 30^\circ$ ) is dependent on total available moisture while  
365 the cool state ( $\lambda = 40^\circ$ ) is not. From Fig 3a, it is clear that the warm states become  
366 warmer with increasing  $Q_{tot}$  at low latitudes. At  $30^\circ$  (Fig 3a),  $T_s$  increases from 306 K to  
367 316 K with  $Q_{tot}$  increasing from 30 to 70 mm. However, at high latitudes (see Fig 3e)  $T_s$   
368 decreases from 274 K to 272 K with  $Q_{tot}$  increasing from 30 mm to 70 mm. Thus, at  $30^\circ$   
369 the final state is “water-limited”: incoming radiation is large and generates large surface  
370 evaporation so that the soil is effectively desiccated. Increasing  $Q_{tot}$  similarly increases  
371 precipitable water, which in turn leads to a strong water vapor greenhouse effect  
372 causing  $T_s$  to increase. At high latitudes ( $\lambda = 40^\circ$ ) nearly all available water in the  
373 system resides in the soil, leaving the atmosphere nearly devoid of moisture. This  
374 corresponds to an “energy-limited” regime: TOA incoming insolation is insufficient to  
375 generate substantial surface evaporation (or latent heat release). However, since  $\beta$  is  
376 an increasing function of  $Q_{soil}$ ,  $Q_{soil}$  increases evaporation, which ultimately increases  
377 precipitable water. Under cold conditions, the humidity profile is very close to saturation;  
378 hence, even a small increase of precipitable water induces more low-level clouds, which  
379 reduces incoming surface shortwave radiation and results in a (small) decrease of  $T_s$ .

380 To summarize, the sensitivity of RCE states to changes in total water content is:  
381 (i) of opposing sign for high and low latitudes, and (ii) of larger magnitude at low  
382 latitudes. Such differential sensitivity can be explained through distinct responses of the  
383 atmospheric radiative properties to changes in precipitable water. Low incoming  
384 radiation induces cold conditions and high relative humidity, which strengthens low-level

385 cloud cover and cloud optical thickness. High incoming radiation induces warm  
386 conditions associated with increased precipitable water.

387         Apart from the extreme latitudes, intermediate solutions (Fig 3 green symbols)  
388 and multiple equilibria are found to occur at all other latitudes considered (see Fig 3b,c  
389 and d). These intermediate RCE states are associated with water being more equitably  
390 partitioned between the soil and the atmosphere ( $Q_{soil} > 5$  mm and  $W > 5$  mm). In these  
391 experiments, the multiple equilibria appear to be either bimodal or trimodal. For  
392 intermediate latitudes, there is an optimum range of  $Q_{tot}$  that favors multimodal solutions  
393 and the intermediate RCE states. Fig 3 shows that, for  $Q_{tot} = 30$  mm (i.e  $Q_0 = 5$  mm), it  
394 is not possible to reach an intermediate RCE state for any of the latitudes considered  
395 (i.e., green symbols are absent). Only warm and cool equilibria are present for  
396 intermediate latitudes. Low values of  $Q_{tot}$  appear to favor bimodality (warm and cool  
397 states) rather than multimodality (warm, intermediate and cool). At large total water  
398 content,  $Q_{tot} = 70$  mm, the multiple equilibria disappear (see Fig 3d), as the model tends  
399 to a cool RCE state regardless of the initial condition. In conclusion, we note here an  
400 “optimum” range of  $\lambda$  (energy) and  $Q_{tot}$  (water) values that allow intermediate states with  
401 neither a completely dry, desert-like, nor fully wet, swamp-like, surface. This range  
402 corresponds to a regime that is neither “energy-limited” (in terms of solar radiation) nor  
403 “water-limited” (in terms of total water content). Within this range, the coupled land-  
404 atmosphere SCM system exhibits multimodal RCE states.

#### 405 4. Investigation of equilibria states (dry, wet and intermediate):

##### 406         Sensitivity to latitude and the role of clouds

#### 407        **4.1. Diagnosis of RCE state dependence on latitude:**

408            To understand the characteristics of the RCE states, including the genesis of  
409 multiple equilibria, we consider here how the system evolves toward these states at  
410 different latitudes. To do so, we focus on the simulations with  $Q_{tot} = 60$  mm and  $T_0 =$   
411 280K. From Fig 3, we note that this set of conditions gives the range of RCE states—  
412 warm, cool and intermediate—over  $30^\circ$  to  $40^\circ$ .

413            Fig 5 depicts 10-day moving averages of the time series of surface temperature,  
414 soil water content, precipitation and precipitable water at each latitude. For all latitudes  
415 except  $30^\circ$  these variables reach a steady state after  $\sim 1$  year. On the other hand, for  
416  $\lambda = 30^\circ$  there is a transient regime comparable to the one observed in Fig 1. The  
417 coupled land-atmosphere system exhibits large, quasi-periodic, oscillations at the  
418 monthly time scale (rather than the single big jump observed in Fig 1a) during the first  
419 half of the simulation and then smoothly converges towards its stable solution. The  
420 coupled land-atmosphere system is capable of producing internal variability that can  
421 cause transitions from one equilibrium state to another one. Fig 5 also shows that the  
422 nontrivial latitude dependence of these variables. The warm ( $\lambda = 30^\circ$ ) and cool solutions  
423 ( $\lambda = 37.5^\circ$  and  $40^\circ$ ) are clearly distinguishable, whereas the two intermediate RCE  
424 states ( $\lambda = 32.5^\circ$  and  $\lambda = 35^\circ$ ) are quite close to each other, with equilibrium surface  
425 temperatures of 297.5 K and 295 K for  $\lambda = 32.5^\circ$  and  $\lambda = 35^\circ$ , respectively.

426            The (surface) precipitation rate provides an indication of the intensity of the  
427 hydrologic cycle at equilibrium: it is equal to the surface evapotranspiration when RCE  
428 is reached. The latitude dependence of surface precipitation is not only nonlinear but  
429 also non-monotonic, as it increases from a minimum value  $\lambda = 30^\circ$  (1.2 mm/day) to a

430 peak value at  $\lambda = 32.5^\circ$  ( $\sim 2.85$  mm/day) and then decreases toward higher latitudes. In  
431 the next subsection, we present and discuss mean vertical profiles at equilibrium to  
432 elucidate the behavior of precipitation with latitude.

#### 433 **4.2. Mean Vertical profiles:**

434 Mean vertical profiles of heating tendencies, relative humidity, and precipitation  
435 averaged over the last three months of the simulation are depicted in Fig 6. The heating  
436 tendencies (Fig 6a) elucidate some important characteristics of the RCE states,  
437 including the strength and depth of convection. RCE is found to hold at essentially every  
438 point in the vertical, as, on average, turbulent diffusion, shallow and deep convection  
439 heating compensates radiative cooling at each level. It is interesting to point out that  
440 some RCE solutions manifest similar column-integrated tendencies but with very  
441 different vertical heating profiles. Consequently, a continental RCE state is better  
442 defined by its surface temperature and soil moisture (or precipitable water) state, rather  
443 than by its column-integrated radiative cooling (or convective heating). According to Fig  
444 6a, the principal differences in the radiative heating vertical distribution among the  
445 different equilibria, and thus in the convective heating profiles, are readily seen in the  
446 vertical extent of the radiative convective instability, with both convection height and  
447 strength decreasing with latitude. For the cool-wet and warm-dry cases, the respective  
448 convection heights are  $\sim 300$  hPa and  $\sim 150$  hPa. This result is consistent with the  
449 monotonic decrease of the average surface temperature with latitude, which exerts a  
450 strong control on convection depth via control of the moist adiabatic temperature profile  
451 (Larsson & Hartmann, 2005). Larsson and Hartmann (2005) argue that the altitude at

452 which radiative cooling drops to zero determines the anvil top, i.e. the cloud top  
453 detrainment zone.

454         Apart from the overall profile vertical extent, the largest heating tendency  
455 differences across the latitude range occur around the 750 hPa level and near the  
456 surface. At 37.5° and 40°, a peak in net radiative cooling is present at 600 hPa and is  
457 associated with net radiative heating immediately below. This radiative heating dipole is  
458 not present at the other latitudes. For  $\lambda = 35^\circ$  and  $37.5^\circ$ , intense radiative cooling  
459 occurs in the lowermost atmospheric layer. In subsection 4.3, we demonstrate that  
460 these features in the radiative heating profiles are related to the vertical distribution of  
461 cloudiness.

462         The mean vertical profiles of relative humidity (Fig 6b) and precipitation (Fig 6c)  
463 are also useful for distinguishing RCE states, as they clearly show daily-mean boundary  
464 layer depth, cloud top, and levels of rainfall generation and re-evaporation. Starting from  
465 the surface, the first peak in relative humidity indicates the daily-mean boundary layer  
466 depth, or the daily-mean cloud base, while the second peak indicates the daily-mean  
467 cloud top. At  $\lambda = 30^\circ$ , the boundary layer is significantly drier and higher than in other  
468 cases because of both the large surface sensible heat flux and boundary layer top dry  
469 air entrainment. Rain re-evaporation in the subcloud layer is, in turn, dramatically  
470 increased (Fig 6c, red curve). Consideration of the vertical profiles of precipitation points  
471 to the source of the maximum surface rain simulated  $\lambda = 32.5^\circ$ . In particular, the vertical  
472 structure suggests a tradeoff between convection maximum strength and rain re-  
473 evaporation beneath cloud base. With increasing insolation, the vertical profile of  
474 convective heating shifts upward and strengthens. Thus, the maximum rain rate rises

475 monotonically from  $\sim 1.7$  mm/day at 750 hPa for  $\lambda = 40^\circ$  to  $\sim 4.7$  mm/day at 600 hPa  
476 for  $\lambda = 30^\circ$  (see Fig 6c). On the other hand, rain re-evaporation increases as the cloud  
477 base rises. Thus, for the warmest case, the rain rate decreases from 4.7 mm/day at 600  
478 hPa to 1.2 mm/day at the surface. In summary, convection strengthens as latitude  
479 decreases but boundary layer deepening and drying enhances evaporative cooling in  
480 the lower atmosphere. This strong evaporative cooling fuels very intense unsaturated  
481 downdrafts that spread at the surface as density currents (not shown).

482 In the cool cases ( $\lambda = 37.5^\circ$  and  $\lambda = 40^\circ$ ) relative humidity is larger although there  
483 is much less precipitable water than in other cases (see Fig 5). From the surface to the  
484 cumulonimbus top, relative humidity always exceeds 50% because the atmosphere is  
485 so cold that the partial pressure of saturation is low. Intermediate solutions ( $\lambda = 32.5^\circ$   
486 and  $\lambda = 35^\circ$ ) exhibit very similar vertical profiles of relative humidity and precipitation,  
487 with little difference in the convection depth.

488 The three families of continental RCE states thus exhibit very distinct vertical  
489 profiles. Each one of the preferred states seems to correspond to a particular vertical  
490 structure of the atmosphere. The next subsection investigates the role of clouds in the  
491 establishment of these three families of solutions.

### 492 **4.3. Cloud cover**

493 The mean diurnal cycle of the vertical distribution of cloud fraction at equilibrium  
494 are displayed in Fig 7. Total cloud cover, especially low-level cloud over, increases with  
495 latitude. Oppositely, cloud top decreases with latitude, in agreement with the decreasing  
496 vertical extent of moist convection. During the daytime, cloud amount is also maximized

497 because of moist convection. More importantly, cloud fractions clearly reveal the 3  
498 different RCE types: warm, intermediate and cool.

499 In the warm case ( $\lambda = 30^\circ$ , Fig 7a) cloud amount is low. Cumulus cloud base  
500 rises from 800 hPa to 700 hPa from 1000 LT to 1400 LT, while cumulonimbus cloud top  
501 is located around 150 hPa and exhibits the strongest cloud fraction between 1300 LT  
502 and 1800 LT. In the LMDZ5B SCM, cumulus clouds are located at the detrainment zone  
503 of moist thermal plumes originating from the surface. When triggered, deep convection  
504 generates deep cumulonimbus that transports heat and moisture from the lower free  
505 troposphere to its top. In the model, the sudden disappearance of shallow cumuli  
506 synchronized with deep convection initiation is due to precipitation. Indeed, once deep  
507 convection is triggered, heavy rainfall and associated cold pools fed by unsaturated  
508 downdrafts tend to cool and stabilize the boundary layer (Tompkins 2001a,b; Grandpeix  
509 et al. 2010; Grandpeix and Lafore 2010). This stabilization likely accounts for the  
510 sudden disappearance of low-level clouds in the mid-afternoon, despite the fact that  
511 convective precipitation is still present. Then, the time lag between low- and high-level  
512 clouds illustrates the succession between shallow and deep convective regimes in all  
513 cases listed in Fig 7. However, we point to the shorter duration of convective events in  
514 the warm cases. In summary, two successive cloud layers characterize the warm RCE  
515 states: a cumulus layer followed by a cirrus layer collocated with the cumulonimbus  
516 cloud detrainment zone. They exert a net positive radiative forcing in the underlying  
517 atmosphere and at the surface (Bony et al. 2004; Bony and Dufresne 2005; Bony et al.  
518 2006). We shall notice the absence of mid-level clouds. This lack of mid-level clouds is

519 a long-standing issue in LMDZ as in many GCMs, which is related to the  
520 misrepresentation of congestus clouds.

521 Intermediate states ( $\lambda = 32.5^\circ$  and  $\lambda = 35^\circ$ , Fig 7b and 7c) are characterized by the  
522 presence of three distinct cloud layers: (i) a high one at the anvil top, (ii) a low one,  
523 which corresponds to the development of a shallow cumulus layer prior to deep  
524 convective onset, and (iii) a third one just above the surface that corresponds to  
525 morning fog occurring between 0300 LT and 0900 LT. This foggy layer represents a  
526 distinct behavior from an oceanic boundary, since it is generated by rapid nocturnal  
527 cooling of the surface, which leads to the a low condensation point observed in Fig 6a  
528 (yellow and green curves) near the surface. This condensed layer is thus mostly  
529 induced by the diurnal evolution of the land surface energy budget and especially by its  
530 nighttime cooling, unlike stratocumuli over the ocean, which are induced by a  
531 combination of surface latent heat flux, a shallow boundary layer, and large-scale  
532 subsidence. This condensed layer plays a very important role in cooling the lower  
533 atmosphere by reflecting incoming sunlight. The layer delays sunlight surface heating  
534 and the morning deepening of the boundary layer, thereby modulating the entire diurnal  
535 cycle of convection. We shall notice that the absence of surface wind in our experiments  
536 favors the development and persistence of morning fog. In section 5 we evaluate the  
537 effect of wind on the RCE. At about 0900 LT, the fog disappears and shallow convection  
538 starts. Associated cumulus clouds develop until the deep convective onset, at around  
539 1500 LT. Deep convection activity lasts for about 6 hours.

540 For cool RCE states (i.e.  $\lambda = 37.5^\circ$  and  $40^\circ$ , Fig 7d and 7e), the succession of  
541 shallow and deep regimes is less obvious. A permanent stratocumulus layer is present

542 at 750 hPa, which cools the lower atmosphere and strongly limits cumulus and  
543 cumulonimbus development. In the LMDZ5B SCM, this permanent cloud layer is  
544 collocated with turbulent motions associated with strong destabilization generated by  
545 cloud top radiative cooling. Indeed, this cloud layer is nearly opaque to both incoming  
546 shortwave radiation and outgoing longwave radiation (Wood 2012), explaining the  
547 strong radiative cooling peak near cloud top (750 hPa) observed in Fig 6a (light blue  
548 and blue curves). This dense cloud layer also traps longwave radiation in the lower  
549 atmosphere, leading to net radiative heating around 850 hPa (see Figure 5a). The  
550 second peak is located much higher, between 500 hPa and 250 hPa, and corresponds  
551 to the anvil cloud top. However, the cirrus radiative feedback is not sufficient to balance  
552 the strong surface cooling induced by the permanent stratocumulus layer.

553 In summary, in the cool RCE state, the atmosphere is so cold that the low  
554 saturation partial pressure is associated with large relative humidity values. The high  
555 relative humidity in turn favors the presence of a permanent low-level cloud layer, which  
556 is nearly opaque to daytime shortwave radiation heating of the surface and ultimately  
557 maintains the system in a cold state. The system is then locked into a very stable  
558 regime. Analogous stable, cold, and cloudy states have been found in other studies  
559 using SCMs such as the CFMIP-GASS Intercomparison of LES and SCM models  
560 (CGILS) (Zhang et al. 2012), which sought to enhance understanding of the transition  
561 from stratocumulus to cumulus regimes. Brient (2011) found that adding stochastic  
562 noise to the vertical motion field greatly improves an SCM's capacity to mimic the  
563 observed cloud cover vertical distribution. This suggests that maintaining a constant  
564 vertical wind velocity, as is the case here may favor "locked" cloudy regimes in SCMs.

#### 565 **4.4. Summary:**

566 To summarize the results, we have shown that the coupled land-atmosphere  
567 system supports multiple RCE states and can exhibit multiple equilibria based on the  
568 initial temperature of the system. The final equilibrium states fall into three main  
569 categories: i) cool and wet surface, ii) warm and dry surface, and ii) intermediate  
570 temperature and moisture regimes. Each state corresponds to a stable cloud regime.  
571 Clouds and their interaction with radiation are suspected to play a key role in the  
572 establishment and maintenance of these equilibrium states. Each type of RCE  
573 corresponds to a certain vertical and temporal distribution of cloudiness: a 2- layer  
574 (daytime cumulus and evening cirrus) configuration for warm RCEs, a 3-layer  
575 configuration (morning fog, daytime cumulus and evening cirrus) for intermediate RCEs,  
576 and a 3-layer configuration (permanent stratocumulus, daytime cumulus and evening  
577 cirrus) for cool RCEs. This result holds true for the 125 experiments conducted in  
578 section 3.

#### 579 **5. Role of cloud radiative feedback on multiple equilibria**

580 The relative importance of clouds for the emergence of multiple equilibria is now  
581 evaluated. A sensitivity experiment for the range of  $T_0$  and  $Q_{tot}$  values at  $\lambda=35^\circ$  was  
582 performed without cloud radiative forcing, i.e. clouds were rendered transparent to both  
583 shortwave and longwave radiation. The RCE states for these sensitivity experiments are  
584 plotted in Fig 8. Removing the cloud radiative forcing eliminates multiple equilibria, at  
585 least for the conditions considered here. Moreover, none of the final states exhibits a  
586 warm-dry or a cool-wet RCE, rather, all final states are grouped around  $T_s = 300$  K and

587 water is present in both the soil and atmosphere, as with the intermediate RCE states  
588 described above. Hence, Fig 8 strongly supports the hypothesis that cloud radiative  
589 forcing is a necessary condition for the presence of multiple equilibria. The continental  
590 RCE framework allows a diurnal cycle of surface temperature that naturally introduces  
591 some variability into the system. For instance, the presence of morning fog is  
592 determined by the minimum nighttime surface temperature. Hence, if an internal  
593 perturbation results in a drop in the minimum nocturnal temperature, the morning fog  
594 may appear and delay the surface and atmospheric heating, increasing the probability  
595 of obtaining a colder surface on the following day. Ultimately, the system may fall into a  
596 colder equilibrium. Such a feedback loop involving clouds and radiation is rendered  
597 possible by the presence of the large diurnal variations of surface temperature. In the  
598 following, we attempt to identify the main cloud types contributing to the simulated  
599 nonlinearities and multiple equilibria.

600 We reproduce the sensitivity to latitude experiment conducted in Section 4 under  
601 four different configurations, in order to quantify the relative role of low (i.e. below 600  
602 hPa) and high (i.e over 600 hPa) clouds. The original (fully coupled clouds) experiment  
603 is compared with three other experiments in which: (i) all clouds are transparent to  
604 radiation (see Fig 9b: “no clouds” experiment); (ii) only low clouds interact with radiation  
605 (see Fig 9c: “low clouds only” experiment); and (iii) only high clouds interact with  
606 radiation (see Fig 9d: “high clouds only” experiment). Since the “no-cloud” (Fig 9b) and  
607 “high-cloud only” (Fig 9d) experiments exhibit similar behaviors, we conclude that high-  
608 clouds are not a leading-order source of nonlinearity. Indeed, the equilibrium surface  
609 temperature decreases linearly with latitude when only the high cloud radiative forcing is

610 retained (see Fig 9d). Compared to the “no-cloud” experiment (Fig 9b), high clouds  
611 significantly heat the atmosphere and the surface through their longwave greenhouse  
612 effect. Without the cloud radiative effect, equilibrium surface temperatures ranges from  
613 289 to 308K, whereas inclusion of high-cloud radiative forcing increases this range from  
614 292 to 313K.

615         When only low-cloud radiative forcing is included, the system may be attracted  
616 toward multiple preferred states, similar to what was observed in Figs 5 and 9a.  
617 Therefore we conclude that, within the LMDZ5B SCM, low-level clouds are the main  
618 source of nonlinearity leading to multiple equilibria. Low-level clouds are already known  
619 to be a principal source of GCM spread (Bony et al. 2004; Bony and Dufresne 2005;  
620 Bony et al. 2006); here their importance is further emphasized over land regions  
621 through the prism of the RCE framework. Of course, since LMDZ5B SCM tends to  
622 underestimate mid-level clouds, as do many GCMs, this conclusion should be viewed  
623 with caution. Indeed, undersimulation of mid-level clouds may exaggerate the role of  
624 low-level clouds.

625         Overall, these results underscore clouds as a critical component of the land-  
626 atmosphere system’s nonlinearity, with the diurnal cycle enhancing the internal  
627 variability that allows the presence of multiple equilibria. In the presence of interactive  
628 clouds, the RCE states correspond to distinct cloud vertical distributions as depicted in  
629 Figure 7. Feedback pathways associated with convection, clouds and radiative cooling,  
630 may favor some convective regimes over others. That is, clouds strongly modulate the  
631 radiative cooling profiles with which the convective heating profiles must adjust to obtain

632 RCE. In turn, vertical mixing of heat and moisture induced by moist convection  
633 ultimately leads to cloud formation, which affects radiation.

634 We performed similar experiments with an SCM based on the version of the  
635 LMDZ GCM used for the 4th IPCC assessment (AR4) (Hourdin 2006) to check the  
636 model-dependency of the results (not shown). In this version, multiple equilibria were  
637 less common in the 30° to 40° range of latitudes, and fewer low clouds were observed  
638 in these simulations as well. Indeed, Hourdin (2006) pointed out that an important bias  
639 of the AR4 version of the LMDZ GCM was its inability to represent low-level cumulus  
640 and stratocumulus. The absence of parameterization for coherent boundary layer  
641 structures (thermals) in this model version likely accounts for the lack of simulated  
642 cumulus clouds. At first glance, these results imply that low-level clouds are necessary  
643 for obtaining multiple equilibria, although additional analysis are required to substantiate  
644 this.

645 It is reasonable to consider how much the results presented here may depend on  
646 the details of the model configuration or the assumptions. Clearly, a comparison of  
647 multiple models would be useful in addressing some concerns about model  
648 dependence. Although a complete assessment regarding how model configuration or  
649 assumptions impact the results is beyond the scope of the current study, we reproduced  
650 the 125 experiments listed in section 3 with a wind forcing nudged toward a geostrophic  
651 value of 10 m/s, in order to study the effect of large-scale forcing on the final equilibrium  
652 of the system. The wind profile computation results from the interaction between  
653 horizontal wind and surface roughness, turbulence and thermals. Hence, we introduce  
654 an additional feedback loop into the system: the wind fully interacts with the SCM

655 boundary layer parameterizations (but not deep convection). The resulting wind profile  
656 is constant in the free troposphere ( $V = 10$  m/s) and mimics the Ekman spiral in the  
657 boundary layer, with a parabolic decrease of the wind magnitude resulting in a surface  
658 wind  $V_0 \sim 0.7$  m/s.

659 Fig 10 is the equivalent of Fig 8 with a geostrophic wind forcing. The main  
660 conclusion is that multiple equilibria still exist as long as cloud radiative feedback is  
661 retained. However the number of final equilibria is slightly reduced and the final states  
662 are distinct from the equilibria obtained without wind. In particular, the morning fog  
663 disappears because of the added mechanical forcing which increases surface exchange  
664 and boundary layer entrainment. The disappearance of fog in turn reduces the vertical  
665 degrees of freedom in the cloud distribution and therefore the number of final RCE  
666 states. When clouds are made transparent to radiation, the multiple equilibria again  
667 disappear, similar to the model behavior in the absence of geostrophic wind. Thus, the  
668 interaction between the geostrophic wind and boundary layer processes does not  
669 diminish the importance of clouds, and especially their radiative feedback, as the main  
670 source of internal variability. Finally, comparing Fig 8b with Fig 10b in the absence of  
671 cloud radiative feedback, we observe that the RCE states are very close whether or not  
672 geostrophic wind is present. Indeed, the unique final equilibrium temperature is nearly  
673 300 K in all cases, while soil water content is increased by  $\sim 5$  mm with geostrophic  
674 wind forcing. This strongly suggests that wind influences the final states via cloud  
675 formation. In other words, when clouds are transparent to radiation, the wind stress  
676 does not considerably change the results, and more generally the wind-boundary layer  
677 feedback becomes of secondary importance. Overall, this experiment further supports

678 the key role of cloud-radiation interactions in generating internal variability in the  
679 coupled soil-atmosphere system.

## 680 6. Summary and conclusions

681 In this study we have examined the applicability of RCE over a land surface  
682 using a single column atmosphere version of the LMDZ GCM coupled to an idealized  
683 land surface model. Relative to its oceanic counterpart, the land system has a finite  
684 moisture capacity corresponding to the total water content in the soil and in the  
685 atmosphere since atmospheric transport and runoff are assumed to be zero, i.e. the  
686 hydrologic cycle is locally closed. Over the ranges of latitude and total water content  
687 explored, multiple equilibria can be obtained by varying initial soil temperature. Three  
688 classes of final RCE states are possible, namely: i) a hot state with a hot and dry  
689 surface and most of the system water content residing in the atmosphere; ii) an  
690 intermediate state with water partitioned between the soil and in the atmosphere; and iii)  
691 a cold state with a wet surface and nearly no moisture present in the atmosphere.

692 By considering sensitivity experiments in which boundary layer diurnal cycle and  
693 cloud radiative forcing are disabled, we show how these are necessary for the  
694 occurrence of multiple equilibria in the LMDZ5B SCM and how they determine the  
695 characteristics of the final RCE states. In particular, low-level clouds and fog appear to  
696 play a key role in the presence of multiple equilibria. For low total water content  
697 conditions, the system is bimodal, while increasing total water content allows the  
698 emergence of the RCE states with water in both the soil and atmosphere. These  
699 intermediate states correspond to either two- or three-layer cloud fraction distributions.

700 In two-layer state, the succession of shallow and deep convection during daytime leads  
701 to cumulus and anvil clouds. In the three-layer state, morning fog develops before  
702 shallow convection onset. Above a threshold value for total water content multiple  
703 equilibria are no longer supported, and the system falls into a cold state. High relative  
704 humidity then favors the presence of a permanent, thick layer of low-level clouds.  
705 Outside of the latitude range emphasized here ( $30^{\circ}$ - $40^{\circ}$ ), all water evaporates from the  
706 surface (low latitude hot states), corresponding to a water-limited regime, or precipitates  
707 (high latitude cold states), corresponding to an energy-limited regime.

708 For a model configuration in which low-level clouds are rendered transparent to  
709 radiation, the multiple equilibria disappear, which emphasize the key role of clouds and  
710 of their radiative feedbacks in the land-atmosphere system. Overall our results of the  
711 radiative convective equilibrium over land indicate that the cloud radiative feedback,  
712 interacting with the diurnal cycle of radiation, induces bifurcations in the land-  
713 atmosphere system and therefore determines the equilibrium conditions in the land-  
714 atmosphere system.

715

## 716 **Acknowledgements**

717 BRL and PG acknowledge funding support from NSF-AGS 1035843, PG acknowledges  
718 support from DOE-ASR DE-SC0008720, and AHS acknowledges support from NSF  
719 AGS-1008847. The authors thank Gilles Bellon, Christoph Schär and Bjorn Stevens for  
720 stimulating discussions of this work and three anonymous reviewers for their careful  
721 reading and comments.

722

## REFERENCES:

- 724 Aleina, F. C., M. Baudena, F. D'Andrea, and A. Provenzale, 2013: Multiple equilibria on  
725 planet Dune: climate–vegetation dynamics on a sandy planet. *Tellus B*, **65**, 693,  
726 doi:10.1029/2006RG000217.
- 727 Bastiaanssen, W. G. M., M. Menenti, R. A. Feddes, and A. A. M. Holtslag, 1998: A remote  
728 sensing surface energy balance algorithm for land (SEBAL) - 1. Formulation. *J Hydrol*,  
729 **212-213**, 198–212, doi:10.1016/S0022-1694(98)00253-4.
- 730 Bateni, S. M., and D. Entekhabi, 2012: Relative efficiency of land surface energy balance  
731 components. *Water Resour Res*, **48**, W04510–, doi:10.1029/2011WR011357.
- 732 Bechtold, P., J. Chaboureau, A. Beljaars, A. K. Betts, M. Kohler, M. J. Miller, and J.  
733 Redelsperger, 2004: The simulation of the diurnal cycle of convective precipitation over  
734 land in a global model. *Q J Roy Meteor Soc*, **130**, 3119–3137, doi:10.1256/qj.03.103.
- 735 Betts, A. K., 1973: Non-precipitating cumulus convection and its parameterization. *Q J Roy*  
736 *Meteor Soc*, **99**, 178–196.
- 737 Betts, A. K., 1976: The Thermodynamic Transformation of the Tropical Subcloud Layer by  
738 Precipitation and Downdrafts. *Journal of Atmospheric Sciences*, **33**, 1008–1020,  
739 doi:10.1175/1520-0469.
- 740 Bony, S. and Coauthors, 2006: How well do we understand and evaluate climate change  
741 feedback processes? *J Climate*, **19**, 3445–3482.
- 742 Bony, S., and J. Dufresne, 2005: Marine boundary layer clouds at the heart of tropical cloud  
743 feedback uncertainties in climate models. *Geophys Res Lett*, **32**, L20806,  
744 doi:10.1029/2005GL023851.
- 745 Bony, S., and K. A. Emanuel, 2001: A parameterization of the cloudiness associated with  
746 cumulus convection; Evaluation using TOGA COARE data. *J Atmos Sci*, **58**, 3158–  
747 3183.
- 748 Bony, S., J. L. Dufresne, H. Le Treut, J. J. Morcrette, and C. Senior, 2004: On dynamic and  
749 thermodynamic components of cloud changes. *Clim Dynam*, **22**, 71–86,  
750 doi:10.1007/s00382-003-0369-6.
- 751 Boulet, G., Chehbouni, A., Gentine, P., Duchemin, B., Ezzahar, J., & Hadria, R. 2007:  
752 Monitoring water stress using time series of observed to unstressed surface  
753 temperature difference. *Agricultural and Forest Meteorology*, **146**, 159–172.  
754 doi:10.1016/j.agrformet.2007.05.012
- 755 Brubaker, K., and D. Entekhabi, 1995: An analytic approach to modeling land atmosphere  
756 interaction 1. Construct and equilibrium behavior. *Water Resour Res*, **31**, 619–632.

- 757 Castelli, F., D. Entekhabi, and E. Caporali, 1999: Estimation of surface heat flux and an  
758 index of soil moisture using adjoint-state surface energy balance. *Water Resour Res*,  
759 **35**, 3115–3125.
- 760 Cox, S.K., Mc Dougal, D. S., Randall, D. A. and Schiffer, R. A., 1987: FIRE: the First ISCCP  
761 Regional Experiment. *Bulletin of the American Meteorological Society*, **68**, 114-118
- 762 Cronin, T. W., & Emanuel, K. A. 2013: The climate time scale in the approach to radiative-  
763 convective equilibrium. *J. Adv. Model. Earth Syst*, (in press). doi:10.1002/jame.20049
- 764 Dai, A., 2006: Precipitation characteristics in eighteen coupled climate models. *J Climate*,  
765 **19**, 4605–4630.
- 766 DelSole, T., M. Zhao, and P. A. Dirmeyer, 2009: A New Method for Exploring Coupled  
767 Land-Atmosphere Dynamics. *J Hydrometeorol*, **10**, 1040–1050,  
768 doi:10.1175/2009JHM1071.1.
- 769 Derbyshire, S., I. Beau, P. Bechtold, J. Grandpeix, J. Piriou, J. Redelsperger, and P. M. M.  
770 Soares, 2004: Sensitivity of moist convection to environmental humidity. *Q J Roy*  
771 *Meteor Soc*, **130**, 3055–3079, doi:10.1256/qj.03.130.
- 772 Emanuel, K. A., 1991: A Scheme for Representing Cumulus Convection in Large-Scale  
773 Models. *J Atmos Sci*, **48**, 2313–2335.
- 774 Entekhabi, D., and K. Brubaker, 1995: An analytic approach to modeling land-atmosphere  
775 interaction, 2, Stochastic formulation. *Water Resour Res*, **31**, 633–643.
- 776 Entekhabi, D., I. Rodríguez-Iturbe, and R. L. Bras, 1992: Variability in Large-Scale Water-  
777 Balance with Land Surface Atmosphere Interaction. *J Climate*, **5**, 798–813.
- 778 Findell, K., P. Gentine, and B. Lintner, 2011: Probability of afternoon precipitation in eastern  
779 United States and Mexico enhanced by high evaporation. *Nat Geosci*, **4**, 434–439,  
780 doi:10.1038/NGEO1174.
- 781 Gentine, P., A. A. M. Holtslag, F. D'Andrea, and M. Ek, 2013: Surface and atmospheric  
782 controls on the onset of moist convection over land. *J Hydrometeorol*,  
783 130211131121003, doi:10.1175/JHM-D-12-0137.1.
- 784 Gentine, P., B. Heusinkveld, and D. Entekhabi, 2012: Systematic Errors in Ground Heat  
785 Flux Estimation and Their Correction. *Water Resour Res*, **48**, W09541,  
786 doi:10.1029/2010WR010203.
- 787 Gentine, P., D. Entekhabi, and J. Polcher, 2010: Spectral Behaviour of a Coupled Land-  
788 Surface and Boundary-Layer System. *Bound-Lay Meteorol*, **134**, 157–180,  
789 doi:10.1007/s10546-009-9433-z.
- 790 Gentine, P., J. Polcher, and D. Entekhabi, 2011: Harmonic propagation of variability in  
791 surface energy balance within a coupled soil-vegetation-atmosphere system. *Water*  
792 *resources Research*, **47**, –, doi:10.1029/2010WR009268.

- 793 Gold, E., 1909. The isothermal layer of the atmosphere and atmospheric radiation.  
794 *Proceedings of the Royal Society of London. Series A*, **82**(551), 43-70.  
795
- 796 Goody, R. M., 1949. The thermal equilibrium at the tropopause and the temperature of  
797 the lower stratosphere. *Proceedings of the Royal Society of London. Series A.*  
798 *Mathematical and Physical Sciences*, **197**(1051), 487-505.  
799
- 800 Grandpeix, J. Y., and V. Phillips, 2004: Improved Mixing Representation in Emanuel's  
801 Convection Scheme. *Q J Roy Meteor Soc*, **130**, 3207–3222, doi:10.1256/qj.03.144.
- 802 Grandpeix, J.-Y., and J.-P. Lafore, 2010: A Density Current Parameterization Coupled with  
803 Emanuel's Convection Scheme. Part I: The Models. *J Atmos Sci*, **67**, 881–897,  
804 doi:10.1175/2009JAS3044.1.
- 805 Grandpeix, J.-Y., J.-P. Lafore, and F. Cheruy, 2010: A Density Current Parameterization  
806 Coupled with Emanuel's Convection Scheme. Part II: 1D Simulations. *J Atmos Sci*, **67**,  
807 898–922, doi:10.1175/2009JAS3045.1.
- 808 Guichard, F. and Coauthors, 2004: Modelling the diurnal cycle of deep precipitating  
809 convection over land with cloud-resolving models and single-column models. *Q J Roy*  
810 *Meteor Soc*, **130**, 3139–3172, doi:10.1256/qj.03.145.
- 811 Guo, Z. and Coauthors, 2006: GLACE: The Global Land-Atmosphere Coupling Experiment.  
812 Part II: Analysis. *J Hydrometeorol*, **7**, 611–625.
- 813 Hilbert, D., 1912: Begrundung der elementaren Strahlungstheorie, *Physik Zeitschrift*, **13**,  
814 1056-1064
- 815 Hohenegger, C., P. Brockhaus, C. S. Bretherton, and C. Schaer, 2009: The Soil Moisture-  
816 Precipitation Feedback in Simulations with Explicit and Parameterized Convection. *J*  
817 *Climate*, **22**, 5003–5020, doi:10.1175/2009JCLI2604.1.
- 818 Hourdin, F., F. Couvreux, and L. Menut, 2002: Parameterization of the dry convective  
819 boundary layer based on a mass flux representation of thermals. *J Atmos Sci*, **59**,  
820 1105–1123.
- 821 Hourdin, F., J. Y. Grandpeix, C. Rio, S. Bony, and A. Jam, 2012: LMDZ5B: the Atmospheric  
822 Component of the IPSL Climate Model with Revisited Parameterizations for Clouds and  
823 Convection. *Clim Dynam*, doi:10.1007/s00382-012-1343-y.
- 824 Koster, R. D. and Coauthors, 2006: GLACE: The Global Land-Atmosphere Coupling  
825 Experiment. Part I: Overview. *J Hydrometeorol*, **7**, 590–610.
- 826 Koster, R. D., and M. J. Suarez, 1994: The Components of a Svat Scheme and Their  
827 Effects on a Gcms Hydrological Cycle. Vol. 17 of, *Advances in Water Resources*, 61–  
828 78.

- 829 Laio, F., A. Porporato, L. Ridolfi, and I. Rodríguez-Iturbe, 2001: Plants in water-controlled  
830 ecosystems: active role in hydrologic processes and response to water stress - II.  
831 Probabilistic soil moisture dynamics. *Adv Water Resour*, **24**, 707–723.
- 832 Lintner, B.R., P. Gentine, K.L. Findell, F. D'Andrea, A.H. Sobel, and G.D. Salvucci, 2013:  
833 An idealized prototype for large-scale land-atmosphere coupling. *J. Clim.*, **26**, 2379—  
834 2389, doi:10.1175/JCLI-D-11-000561.1
- 835 Manabe, S., and R. T. Wetherald, 1967: Thermal equilibrium of the atmosphere with a given  
836 distribution of relative humidity. *The Warming Papers: The Scientific Foundation for the*  
837 *Climate Change Forecast*, 94–115.
- 838 Manabe, S., 1969: Climate and ocean circulation 1: The atmospheric circulation and the  
839 hydrology of the Earth's surface. *Mon. Weather Rev.*, **97**, 739-774
- 840 Muller, C. J., P. A. O'Gorman, and L. E. Back, 2011: Intensification of Precipitation  
841 Extremes with Warming in a Cloud-Resolving Model. *J Climate*, **24**, 2784–2800,  
842 doi:10.1175/2011JCLI3876.1.
- 843 Phillips, T. J., & Klein, S. A. 2014. Land-atmosphere coupling manifested in warm-season  
844 observations on the US southern great plains. *Journal of Geophysical Research:*  
845 *Atmospheres (In press)*.
- 846 Porporato, A., F. Laio, L. Ridolfi, and I. Rodríguez-Iturbe, 2001: Plants in water-controlled  
847 ecosystems: active role in hydrologic processes and response to water stress - III.  
848 Vegetation water stress. *Adv Water Resour*, **24**, 725–744.
- 849 Prigent, C., Rochetin, N., Aires, F., Defer, E., Grandpeix, J-Y., Jimenez, C., and Papa, F.,  
850 2011: Impact of the inundation occurrence on the deep convection at continental scale  
851 from satellite observations and modeling experiments. *Journal of the Geophysical*  
852 *Research, Atmosphere*, **116**, D24
- 853 Renno, N., 1997: Multiple equilibria in radiative-convective atmospheres. *Tellus Series A-*  
854 *Dynamic Meteorology And Oceanography*, **49**, 423–438.
- 855 Rio, C., and F. Hourdin, 2008: A thermal plume model for the convective boundary layer:  
856 Representation of cumulus clouds. *J Atmos Sci*, **65**, 407–425,  
857 doi:10.1175/2007JAS2256.1.
- 858 Rio, C., F. Hourdin, F. Couvreux, and A. Jam, 2010: Resolved Versus Parametrized  
859 Boundary-Layer Plumes. Part II: Continuous Formulations of Mixing Rates for Mass-  
860 Flux Schemes. *Bound-Lay Meteorol*, **135**, 469–483, doi:10.1007/s10546-010-9478-z.
- 861 Rio, C., F. Hourdin, J. Y. Grandpeix, and J. P. Lafore, 2009: Shifting the diurnal cycle of  
862 parameterized deep convection over land. *Geophys Res Lett*, **36**, –,  
863 doi:10.1029/2008GL036779.
- 864 Rio, C., J. Y. Grandpeix, F. Hourdin, and F. Guichard, 2012: Control of deep convection by  
865 sub-cloud lifting processes: the ALP closure in the LMDZ5B general circulation model.  
866 *Clim Dynam*, 2271–2292.

- 867 Rodríguez-Iturbe, I., A. Porporato, L. Ridolfi, V. Isham, and D. R. Cox, 1999: Probabilistic  
868 modelling of water balance at a point: the role of climate, soil and vegetation. *P R Soc*  
869 *A*, **455**, 3789–3805.
- 870 Rodríguez-Iturbe, I., D. Entekhabi, and R. L. Bras, 1991a: Nonlinear Dynamics of Soil-  
871 Moisture at Climate Scales .1. Stochastic-Analysis. *Water resources Research*, **27**,  
872 1899–1906.
- 873 Rodríguez-Iturbe, I., D. Entekhabi, J. LEE, and R. L. Bras, 1991b: Nonlinear Dynamics of  
874 Soil-Moisture at Climate Scales .2. Chaotic Analysis. *Water resources Research*, **27**,  
875 1907–1915.
- 876 Romps, D. M., 2011: Response of Tropical Precipitation to Global Warming. *J Atmos Sci*,  
877 **68**, 123–138, doi:10.1175/2010JAS3542.1.
- 878 Rossow, W. B., and R. A. Schiffer, 1999: Advances in understanding clouds from ISCCP.  
879 *Bull. Amer. Meteor. Soc*, **80**, 2261–2287.
- 880 Schlemmer, L., C. Hohenegger, J. Schmidli, C. S. Bretherton, and C. Schaer, 2011: An  
881 Idealized Cloud-Resolving Framework for the Study of Midlatitude Diurnal Convection  
882 over Land. *J Atmos Sci*, **68**, 1041–1057, doi:10.1175/2010JAS3640.1.
- 883 Seneviratne, S. I., T. Corti, E. L. Davin, M. Hirschi, E. B. Jaeger, I. Lehner, B. Orlowsky, and  
884 A. J. Teuling, 2010: Investigating soil moisture-climate interactions in a changing  
885 climate: A review. *Earth-Sci Rev*, **99**, 125–161, doi:10.1016/j.earscirev.2010.02.004.
- 886 Simpson, J., and V. Wiggert, 1969: Models of Precipitating Cumulus Towers. *Mon Wea*  
887 *Rev*, **97**, 471–489.
- 888 Tompkins, A. M., 2001a: Organization of Tropical Convection in Low Vertical Wind Shears:  
889 The Role of Water Vapor. *J Atmos Sci*, **58**, 529–545, doi:10.1175/1520-0469(2001)058.
- 890 Tompkins, A. M., 2001b: Organization of Tropical Convection in Low Vertical Wind Shears:  
891 The Role of Cold Pools. *J Atmos Sci*, **58**, 1650–1672, doi:10.1175/1520-  
892 0469(2001)058.
- 893 Tompkins, A. M., and G. C. Craig, 1998a: Time-scales of adjustment to radiative-convective  
894 equilibrium in the tropical atmosphere. *Q J Roy Meteor Soc*, **124**, 2693–2713,  
895 doi:10.1002/qj.49712455208.
- 896 Tompkins, A. M., and G. C. Craig, 1998b: Radiative–convective equilibrium in a three-  
897 dimensional cloud-ensemble model. *Q J Roy Meteor Soc*, **124**, 2073–2097,  
898 doi:10.1002/qj.49712455013.
- 899 Wang, G. and Eltahir, E., 2000: Biosphere-atmosphere interactions over West Africa II:  
900 Multiple climate equilibria. *Q J Roy Meteor Soc.*, **126**, 1261-1280
- 901 Wood, R., 2012: Stratocumulus Clouds. *Mon Wea Rev*, **140**, 2373–2423,  
902 doi:10.1175/MWR-D-11-00121.1.

903 Zhang, M., C. S. Bretherton, and P. N. Blossey, 2012: The CGILS experimental design to  
904 investigate low cloud feedbacks in general circulation models by using single-column  
905 and large-eddy simulation models. *Journal of Advances in Modeling Earth Systems-*  
906 *Discussion*, **4**, doi:10.1029/2012MS000182.

907

## 908 FIGURE CAPTION LIST:

909 Fig 1: Time-series of a) daily average integrated radiative cooling (blue) and convective  
910 heating (red), 10-day running mean b) atmospheric (solid) and soil (dashed) energy  
911 budget and c) surface temperature for the CTL run ( $\lambda = 35^\circ$ ,  $Q_{tot} = 40$  mm and  $T_0 =$   
912 300 K).

913 Fig 2: Averaged diurnal cycle over the last three months of a) Surface temperature, b)  
914 Precipitation, c) atmosphere (black solid) and soil (black dashed) energy budget  
915 (black solid), turbulent fluxes (green), and solar forcing (red), d) vertically integrated  
916 convective (red) and radiative (blue) heating decomposed in its short wave (circle  
917 line) and long wave (dashed lines) components for the CTL run ( $\lambda = 35^\circ$ ,  $Q_{tot} = 40$   
918 mm and  $T_0 = 300$  K).

919 Fig 3: Average surface temperature  $T_s$  (K) versus soil water content  $Q_{soil}$  (mm) ( $Q_{soil} = Q_{tot} -$   
920  $W$ ) over the last three months at different latitudes, for initial soil water content  $Q_0 =$   
921 5 mm (circles), 15 mm (squares), 25 mm (triangles), 35 mm (diamonds) and 45 mm  
922 (stars). Grey arrows link the initial state to the final state. The “cool states”  
923 (maximum  $Q_{soil}$  and minimum  $T_s$ ) are highlighted in blue, the “warm states” ( $Q_{soil} \sim 0$   
924 and maximum  $T_s$ ) in red, and the “intermediate states” in green ( $0 < Q_{soil} < Q_{max}$  and  
925  $T_{min} < T_s < T_{max}$ ). The black squares indicate the points families owing to the same  
926 equilibrium state (or attractor). Multiple equilibria are present when a group of

927 arrows originating from the same horizontal line do not converge towards the same  
928 attractor. Green symbols that are not squared can correspond to RCE either (1) still  
929 not in a steady regime (i.e Net (TOA) different from zero) (2) or may be trapped into  
930 an intermediate RCE state that is (i) not shared by any other RCE of this set of  
931 experiment (e.g if differences in  $T_0$  are too large between two experiments), or (ii)  
932 unique.

933 Fig 4: Average surface temperature  $T_s$  (K) over the last three months at different latitudes,  
934 for initial soil water content  $Q_0 = 5$  mm and initial ground temperature  $T_0 = 280$  K  
935 (blue),  $T_0 = 290$  K (light blue),  $T_0 = 300$  K (green),  $T_0 = 310$  K (yellow) and  $T_0 = 320$  K  
936 (red).

937 Fig 5: Time series of 10-day running mean a) surface temperature, b) soil water content, c)  
938 precipitation, and d) precipitable water for  $\lambda = 30^\circ$  (red),  $32.5^\circ$  (yellow),  $35^\circ$  (green),  
939  $37.5^\circ$  (light blue) and  $40^\circ$  (blue). Initial ground temperature is  $T_0 = 280$  K and total  
940 water is  $Q_{tot} = 60$  mm (i.e. initial  $Q_0 = 35$  mm).

941 Fig 6: Mean vertical profile over the last three months of a) convective (solid) and radiative  
942 (dashed) heating, b) relative humidity and c) precipitation for  $\lambda = 30^\circ$  (red),  $32.5^\circ$   
943 (yellow),  $35^\circ$  (green),  $37.5^\circ$  (light blue),  $40^\circ$  (blue). Initial ground temperature is  $T_0$   
944  $= 280$  K and total water is  $Q_{tot} = 60$  mm (i.e. initial is  $Q_0 = 35$  mm).

945 Fig 7: Mean diurnal cycle of the cloud fraction over the last three months at different  
946 latitudes. Initial ground temperature is  $T_0 = 280$  K and total water is  $Q_{tot} = 60$  mm  
947 (i.e. initial  $Q_0 = 35$  mm).

948 Fig 8: Average surface temperature  $T_s$  (K) versus soil water content  $Q_{soil}$  (mm) ( $Q_{soil} = Q_{tot} -$   
949  $W$ ) over the last three months a) with fully interactive clouds and b) without cloud

950 radiative effect, for initial soil water content  $Q_0 = 5$  mm (circles), 15 mm (squares),  
951 25 mm (triangles), 35 mm (diamonds) and 45 mm (stars). Grey arrows link the  
952 initial state to the final state. The “cool states” (maximum  $Q_{soil}$  and minimum  $T_s$ ) are  
953 highlighted in blue and the “warm states” ( $Q_{soil} \sim 0$  and maximum  $T_s$ ) are highlighted  
954 in red and “intermediate states” in green ( $0 < Q_{soil} < Q_{max}$  and  $T_{min} < T_s < T_{max}$ ). The  
955 black squares indicate the points families owing to the same equilibrium state (or  
956 attractor). Multiple equilibria are present when a group of arrows originating from the  
957 same horizontal line do not converge towards the same attractor. Green symbols  
958 that are not squared can correspond to RCE either (1) still not in a steady regime  
959 (i.e. Net TOA different from zero) (2) or may be trapped into an intermediate RCE  
960 state that is (i) not shared by any other RCE of this set of experiment (e.g. if  
961 differences in  $T_0$  are too large between two experiments), or (ii) unique. Latitude is  
962 prescribed at  $35^\circ$ .

963 Fig 9: Time series of 10-day running mean surface temperature for  $\lambda = 30^\circ$  (red),  $32.5^\circ$   
964 (yellow),  $35^\circ$  (green),  $37.5^\circ$  (light blue) and  $40^\circ$  (blue) with a) fully interactive clouds,  
965 b) without cloud radiative effect, c) only with low clouds ( $P < 600$  hPa) radiative  
966 effect, and d) only high clouds ( $P > 600$  hPa) radiative effect. Initial ground  
967 temperature is  $T_0 = 280$  K and total water is  $Q_{tot} = 60$  mm (i.e. initial is  $Q_0 = 25$  mm).

968 Fig 10: Same as Fig 8 with a wind forcing nudged towards a geostrophic value of 10 m/s.

969

970

971

972

973

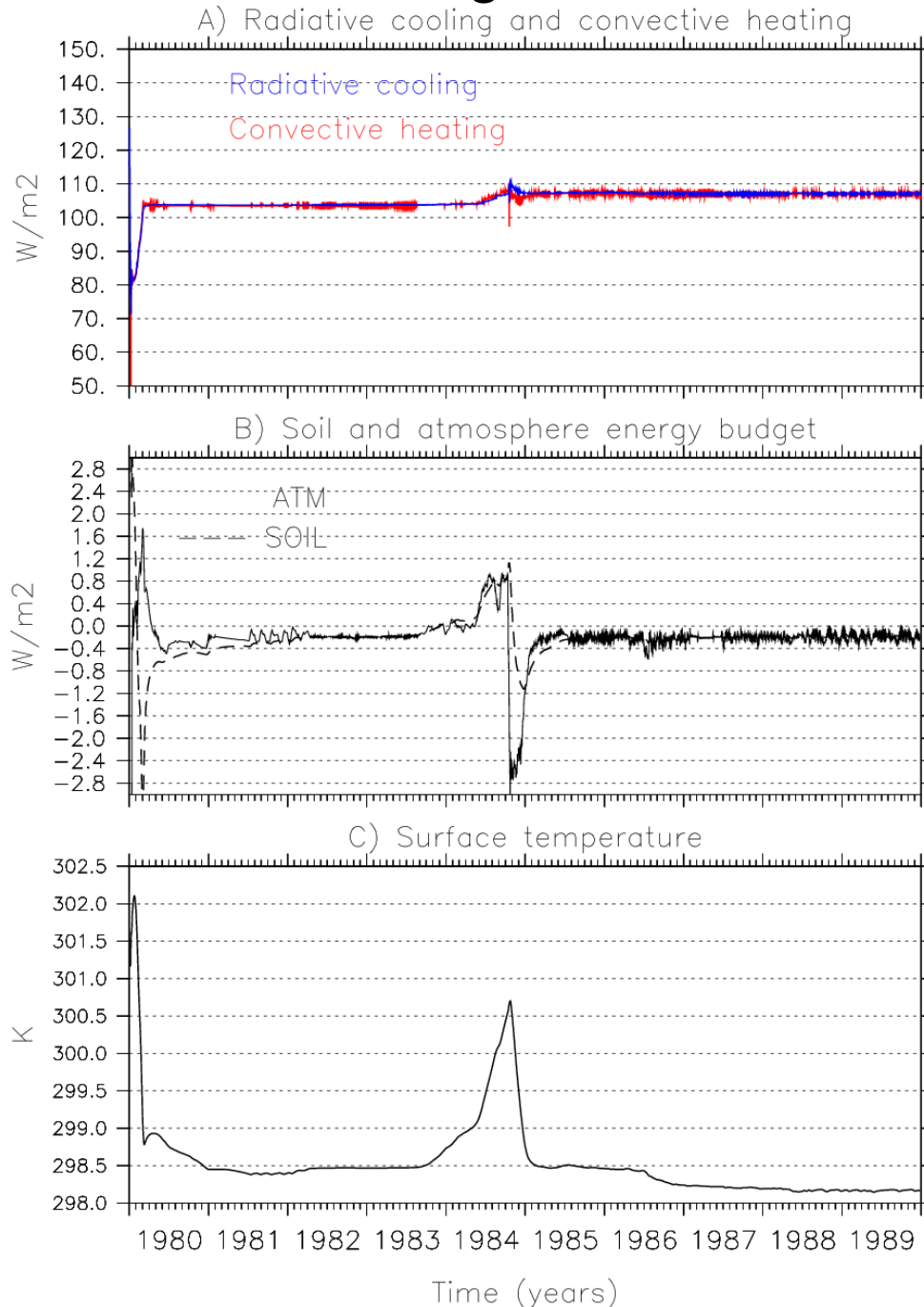
974

975

976

977

# Figures



979

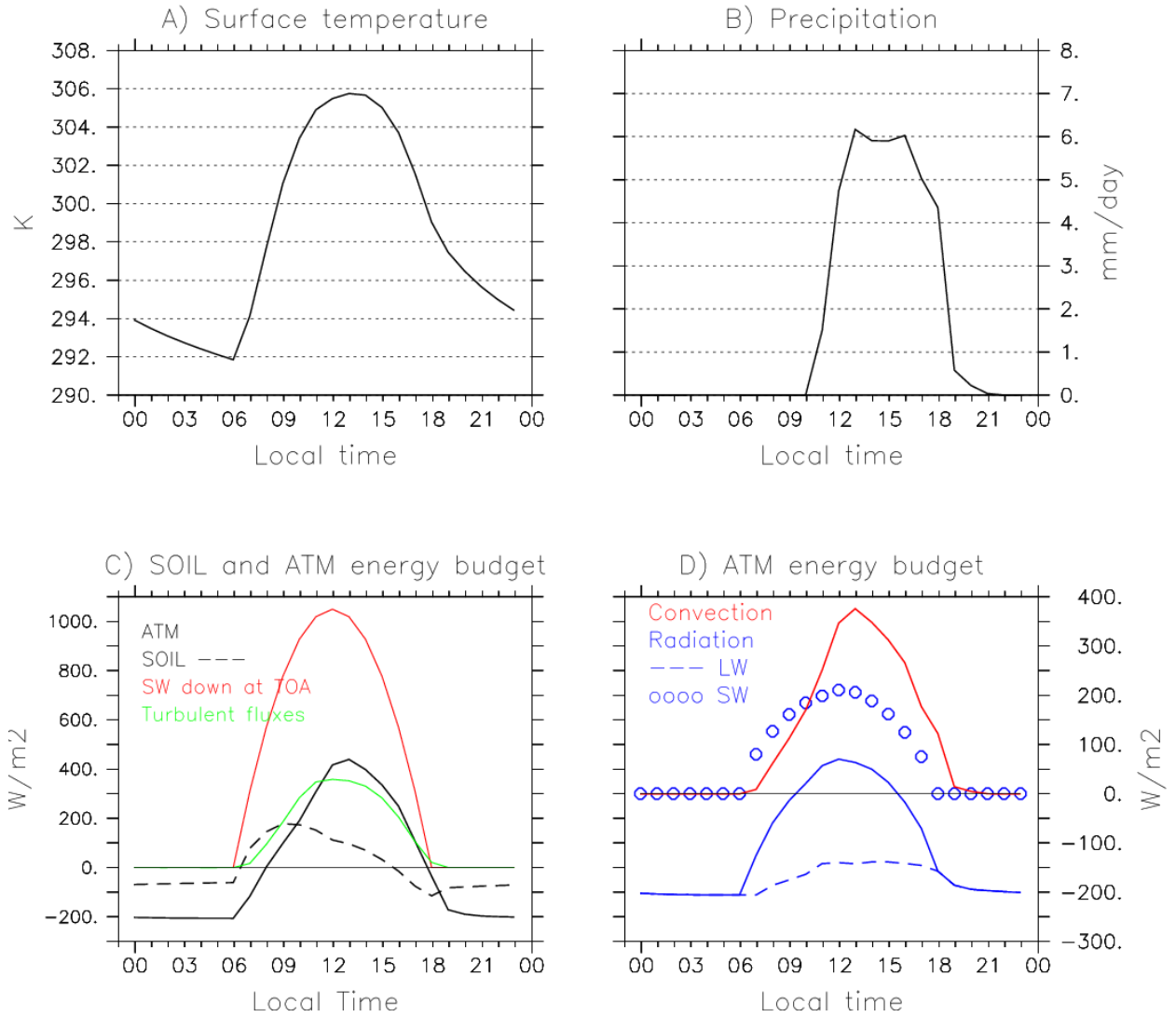
980 **Fig 1:** Time-series of a) daily average integrated radiative cooling (blue) and convective

981 heating (red), 10-day running mean b) atmospheric (solid) and soil (dashed) energy

982 budget and c) surface temperature for the CTL run ( $\lambda = 35^\circ$ ,  $Q_{tot} = 40$  mm and  $T_0 =$ 

983 300 K).

984



985

986 Fig 2: Averaged diurnal cycle over the last three months of a) Surface temperature, b)

987 Precipitation, c) atmosphere (black solid) and soil (black dashed) energy budget

988 (black solid), turbulent fluxes (green), and solar forcing (red), d) vertically integrated

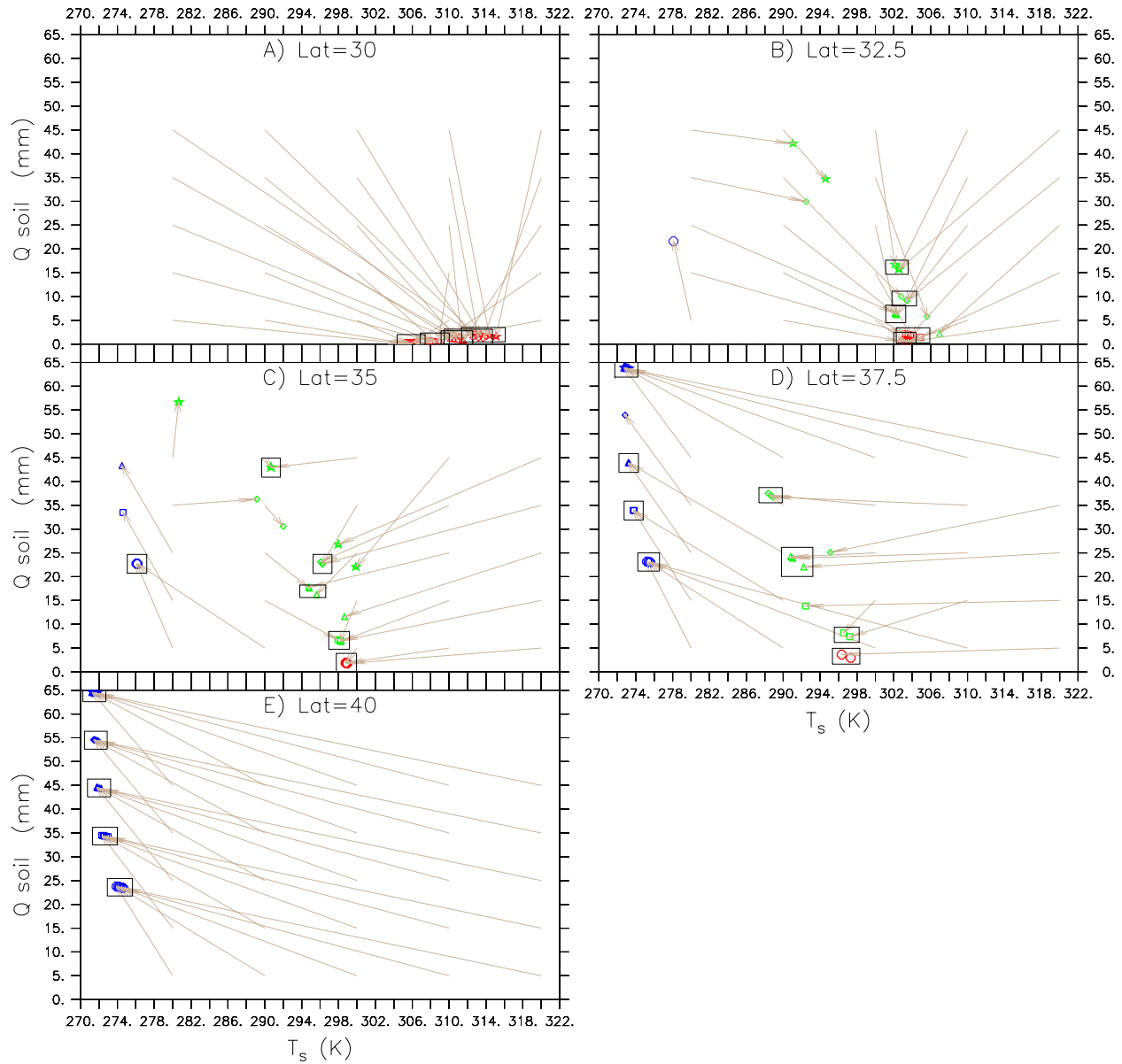
989 convective (red) and radiative (blue) heating decomposed in its short wave (circle

990 line) and long wave (dashed lines) components for the CTL run ( $\lambda = 35^\circ$ ,  $Q_{tot} = 40$  mm

991 and  $T_0 = 300$  K).

992

993



994

995 Fig 3: Average surface temperature  $T_s$  (K) versus soil water content  $Q_{soil}$  (mm) ( $Q_{soil} = Q_{tot} -$   
 996  $W$ ) over the last three months at different latitudes, for initial soil water content  $Q_0 = 5$   
 997 mm (circles), 15 mm (squares), 25 mm (triangles), 35 mm (diamonds) and 45 mm  
 998 (stars). Grey arrows link the initial state to the final state. The “cool states” (maximum  
 999  $Q_{soil}$  and minimum  $T_s$ ) are highlighted in blue, the “warm states” ( $Q_{soil} \sim 0$  and  
 1000 maximum  $T_s$ ) in red, and the “intermediate states” in green ( $0 < Q_{soil} < Q_{max}$  and  $T_{min} <$   
 1001  $T_s < T_{max}$ ). The black squares indicate the points families owing to the same

1002 equilibrium state (or attractor). Multiple equilibria are present when a group of arrows  
1003 originating from the same horizontal line do not converge towards the same attractor.  
1004 Green symbols that are not squared can correspond to RCE either (1) still not in a  
1005 steady regime (i.e Net (TOA) different from zero) (2) or may be trapped into an  
1006 intermediate RCE state that is (i) not shared by any other RCE of this set of  
1007 experiment (e.g if differences in  $T_0$  are too large between two experiments), or (ii)  
1008 unique.

1009

1010

1011

1012

1013

1014

1015

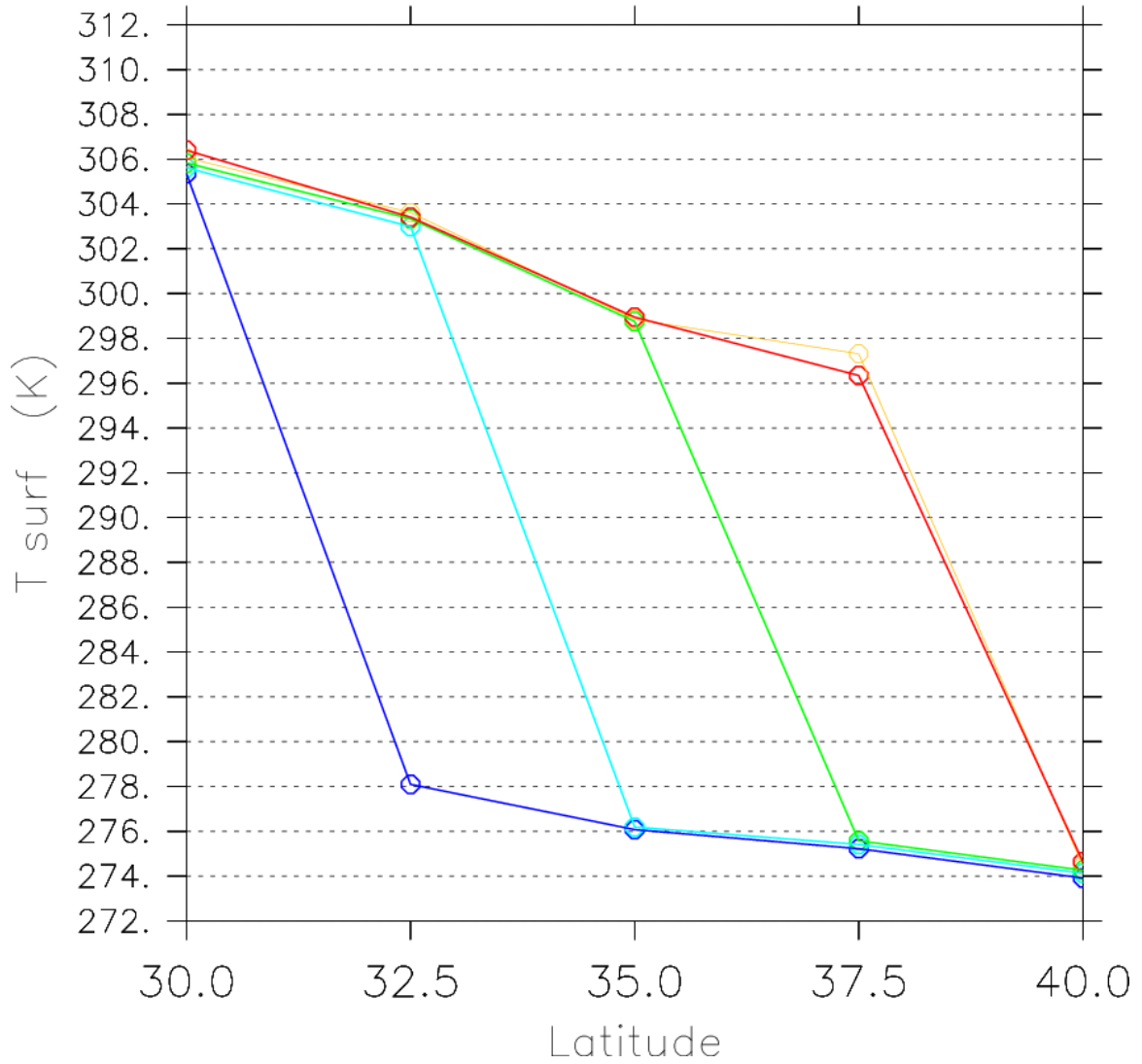
1016

1017

1018

1019

1020



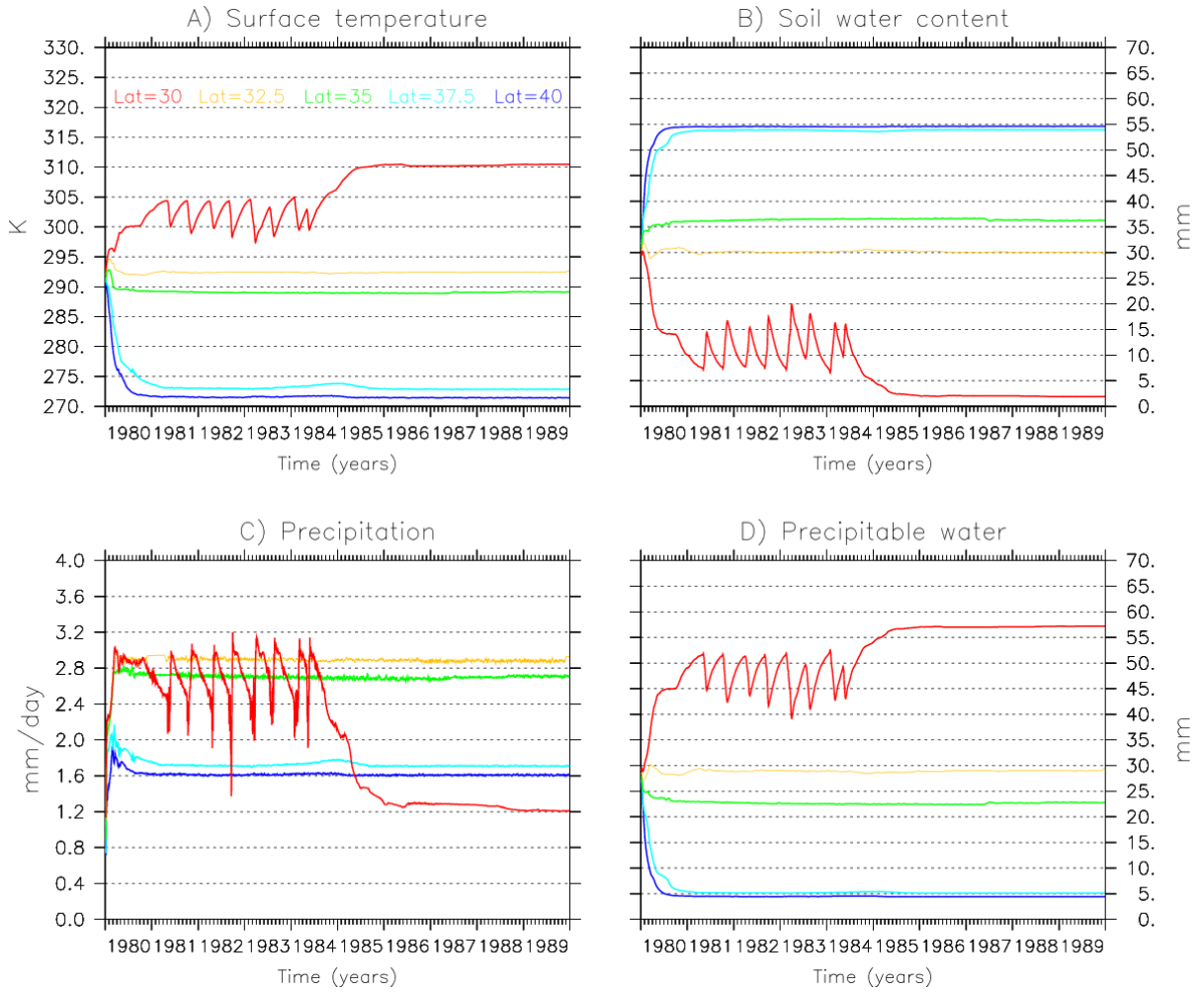
1021

1022 Fig 4: Average surface temperature  $T_s$  (K) over the last three months at different latitudes,  
1023 for initial soil water content  $Q_0 = 5$  mm and initial ground temperature  $T_0 = 280$  K  
1024 (blue),  $T_0 = 290$  K (light blue),  $T_0 = 300$  K (green),  $T_0 = 310$  K (yellow) and  $T_0 = 320$  K  
1025 (red).

1026

1027

1028



1029

1030 **Fig 5:** Time series of 10-day running mean a) surface temperature, b) soil water content, c)  
1031 precipitation, and d) precipitable water for  $\lambda = 30^\circ$  (red),  $32.5^\circ$  (yellow),  $35^\circ$  (green),  
1032  $37.5^\circ$  (light blue) and  $40^\circ$  (blue). Initial ground temperature is  $T_0 = 280$  K and total  
1033 water is  $Q_{tot} = 60$  mm (i.e. initial  $Q_0 = 35$  mm).

1034

1035

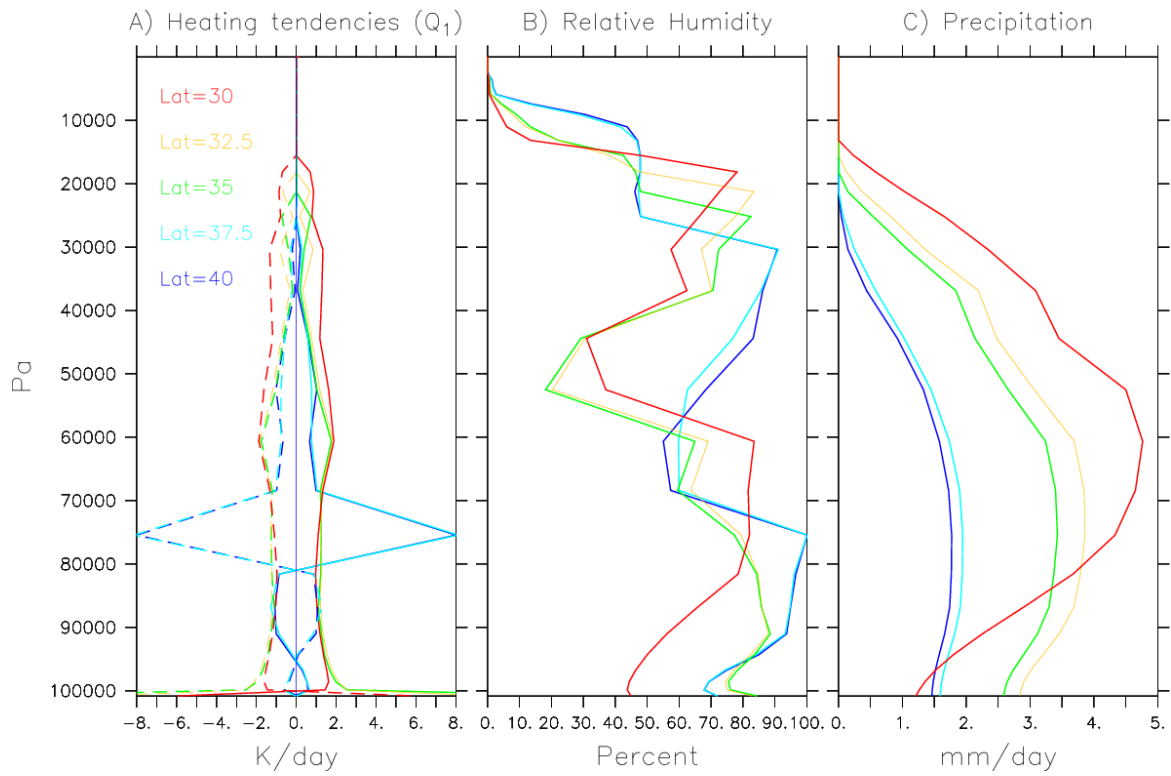
1036

1037

1038

1039

1040



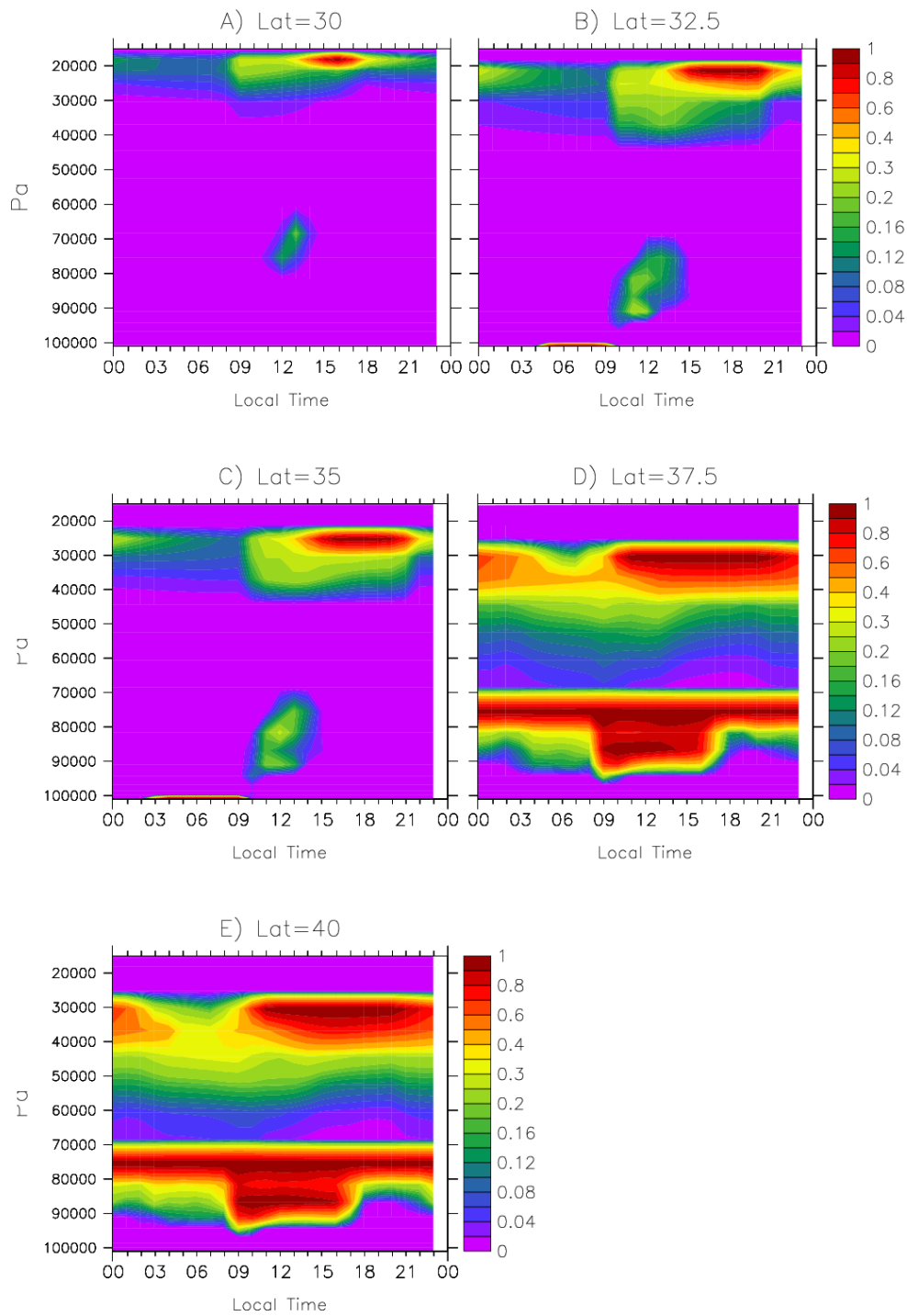
1041

1042 Fig 6: Mean vertical profile over the last three months of a) convective (solid) and radiative

1043 (dashed) heating, b) relative humidity and c) precipitation for  $\lambda = 30^\circ$  (red),  $32.5^\circ$

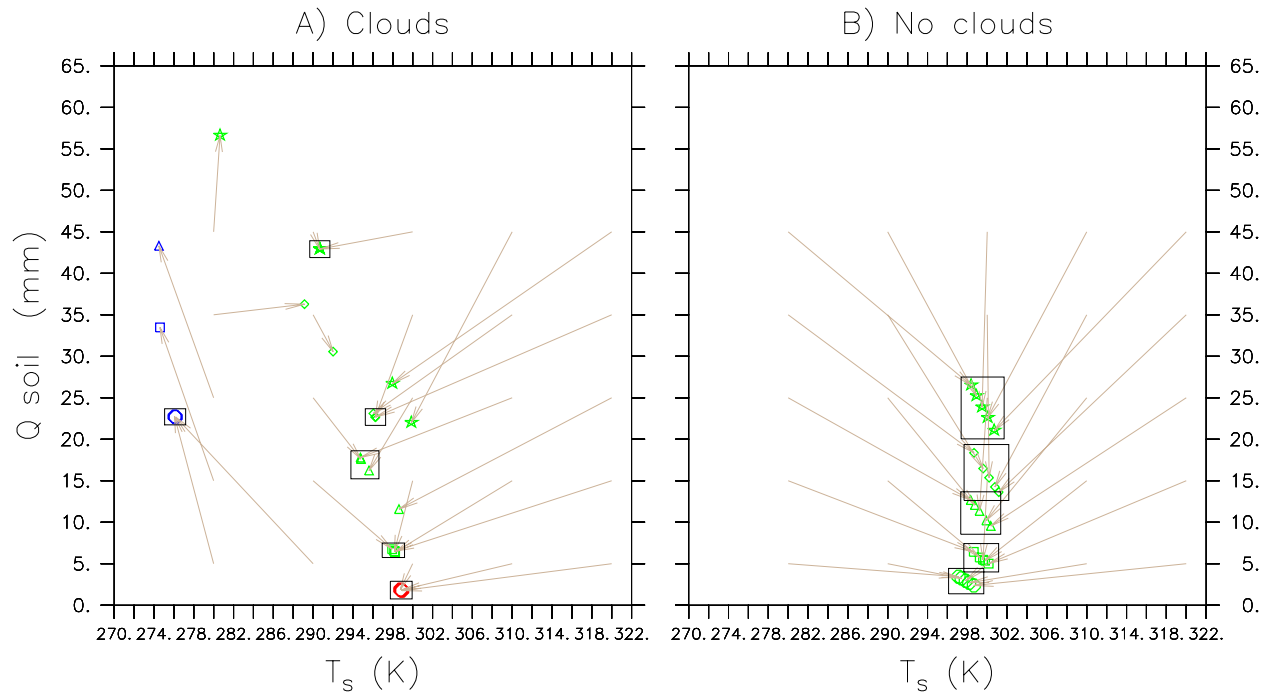
1044 (yellow),  $35^\circ$  (green),  $37.5^\circ$  (light blue),  $40^\circ$  (blue). Initial ground temperature is  $T_0$

1045  $=280$  K and total water is  $Q_{tot} = 60$  mm (i.e. initial is  $Q_0 = 35$  mm).



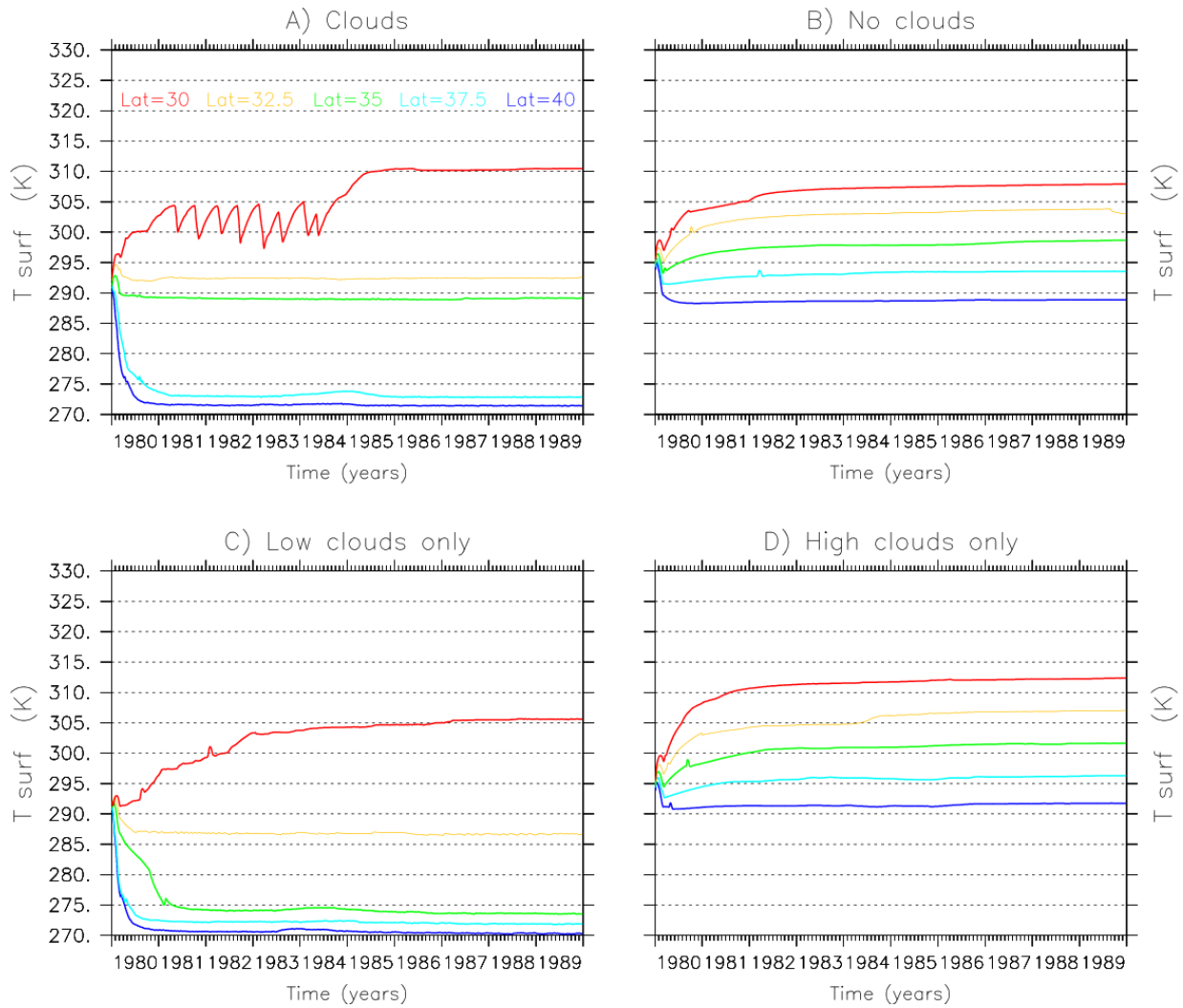
1046

1047 Fig 7: Mean diurnal cycle of the cloud fraction over the last three months at different  
 1048 latitudes. Initial ground temperature is  $T_0 = 280$  K and total water is  $Q_{tot} = 60$  mm (i.e.  
 1049 initial  $Q_0 = 35$  mm).



1050

1051 Fig 8: Average surface temperature  $T_s$  (K) versus soil water content  $Q_{soil}$  (mm) ( $Q_{soil} = Q_{tot} -$   
 1052  $W$ ) over the last three months a) with fully interactive clouds and b) without cloud  
 1053 radiative effect, for initial soil water content  $Q_0 = 5$  mm (circles), 15 mm (squares), 25  
 1054 mm (triangles), 35 mm (diamonds) and 45 mm (stars). Grey arrows link the initial  
 1055 state to the final state. The “cool states” (maximum  $Q_{soil}$  and minimum  $T_s$ ) are  
 1056 highlighted in blue and the “warm states” ( $Q_{soil} \sim 0$  and maximum  $T_s$ ) are highlighted in  
 1057 red and “intermediate states” in green ( $0 < Q_{soil} < Q_{max}$  and  $T_{min} < T_s < T_{max}$ ). The black  
 1058 squares indicate the points families owing to the same equilibrium state (or attractor).  
 1059 Multiple equilibria are present when a group of arrows originating from the same  
 1060 horizontal line do not converge towards the same attractor. Green symbols that are  
 1061 not squared can correspond to RCE either (1) still not in a steady regime (i.e. Net  
 1062 TOA different from zero) (2) or may be trapped into an intermediate RCE state that is  
 1063 (i) not shared by any other RCE of this set of experiment (e.g. if differences in  $T_0$  are  
 1064 too large between two experiments), or (ii) unique. Latitude is prescribed at  $35^\circ$ .



1065

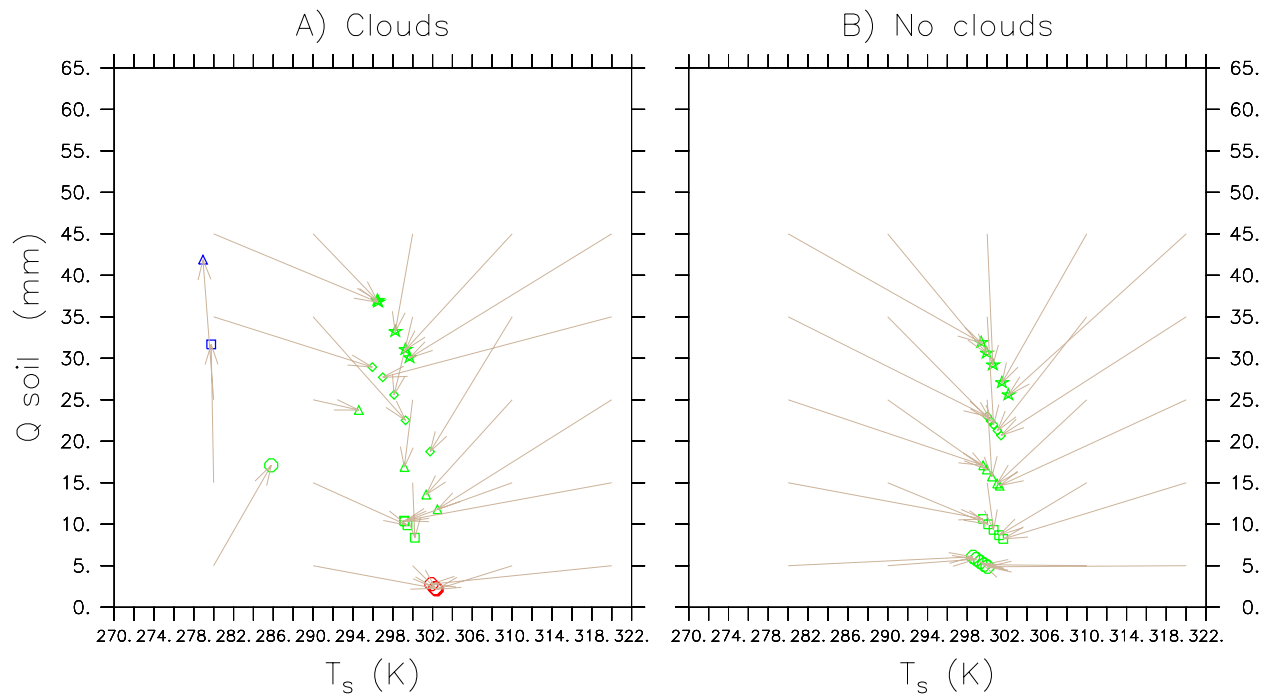
1066 **Fig 9:** Time series of 10-day running mean surface temperature for  $\lambda = 30^\circ$  (red),  $32.5^\circ$   
 1067 (yellow),  $35^\circ$  (green),  $37.5^\circ$  (light blue) and  $40^\circ$  (blue) with a) fully interactive clouds,  
 1068 b) without cloud radiative effect, c) only with low clouds ( $P < 600$  hPa) radiative effect,  
 1069 and d) only high clouds ( $P > 600$  hPa) radiative effect. Initial ground temperature is  $T_0$   
 1070  $= 280$  K and total water is  $Q_{tot} = 60$  mm (i.e. initial is  $Q_0 = 25$  mm).

1071

1072

1073

1074



1075

1076 Fig 10: Same as Fig 8 with a wind forcing nudged towards a geostrophic value of 10 m/s.

1077

1078